Combustion and Flame 163 (2016) 301–316

Contents lists available at ScienceDirect

Combustion and Flame

journal homepage: www.elsevier.com/locate/combustflame

A numerical investigation of the influence of radiation and moisture content on pyrolysis and ignition of a leaf-like fuel element

B.L. Yashwanth [a], B. Shotorban [a,*], S. Mahalingam [a], C.W. Lautenberger [b], D.R. Weise [c]

[a] Department of Mechanical and Aerospace Engineering, The University of Alabama in Huntsville, Huntsville, AL 35899, USA
[b] Reax Engineering Inc., 1958 University Ave., Suite B, Berkeley, CA 94704, USA
[c] Pacific Southwest Research Station, USDA Forest Service, Riverside, CA 92507, USA

ARTICLE INFO

Article history:
Received 27 November 2014
Revised 2 October 2015
Accepted 4 October 2015
Available online 20 November 2015

Keywords:
Computational
Pyrolysis
Live fuels
Cellulose
Ignition

ABSTRACT

The effects of thermal radiation and moisture content on the pyrolysis and gas-phase ignition of a solid fuel element containing high moisture content were investigated using the coupled Gpyro3D/FDS models. The solid fuel has dimensions of a typical *Arctostaphylos glandulosa* leaf which is modeled as thin cellulose subjected to radiative heating on one side. We incorporated a five-step extended Broido-Shafizadeh reaction model for thermal degradation, moisture evaporation, and pyrolysis of cellulose in Gpyro3D. The solid-phase model was successfully validated against published data. Ignition of the modeled leaf-like fuel element at three initial moisture contents (5%, 40%, or 80%) exposed to a 1500 K radiant source was simulated. Lower moisture content resulted in earlier onset of pyrolysis and ignition resulting in higher solid and gas phase temperatures. Local moisture evaporation and temperature rise were observed in all three cases and a significant amount of moisture remained in the sample during ignition. The numerical results suggested that moisture content not only affected the process of pyrolysis, but also influenced the ignition and gas phase combustion of the solid fuel.

1. Introduction

Fire burns in vegetation in many regions of the world; humans and ecosystems have evolved with this process [1]. While wildland fire is a natural and desired ecological disturbance in many areas, it can also pose a threat to human life, property, and natural resources in other areas. The vegetative fuel for wildland fire is a combination of the living plants and their dead, cast-off foliage and branches. These fuel components have a variety of characteristics which influence the pyrolysis, ignition, and subsequent spread of a wildland fire [2]. Of particular importance to fire is the quantity of water contained in the fuel components. Living plants actively regulate the water contained in their plant cells while the dead components absorb and desorb water passively like a sponge [3]. Plants have adapted various strategies to conserve water and the moisture content (mass of water expressed as percentage of dry mass) which ranges from approximately 50% to greater than 300% for some succulents. In contrast, the moisture content of dead fuels ranges from 0% to about 40% at saturation.

Many wildland fires burn in the elevated foliage and branches (collectively known as the plant's crown) of living vegetation. These crown fires burn in coniferous forests in the Northern Hemisphere, eucalyptus forests in Australia, and in shrubland types such as California chaparral, Chilean mattoral, and Mediterranean maquis. In the United States, data used to parameterize the operational model used by wildland fire managers to predict fire spread originated from experiments using dead woody material on the ground. Other empirical models have been developed from observed fire spread in live fuels in the field [4–9]. These operational models [4–6] can predict fire spread rate well for the conditions under which the data were collected, but they are less accurate for other conditions.

Because of its empirical-physical nature, the model developed by Rothermel [4] does not explicitly model heat transfer modes as do other models, e.g., Pagni and Peterson [10] and Balbi et al. [11]. In a spreading wildland fire, fuel particles such as leaves and branches in unburnt vegetation are exposed to convective and radiative heat transfer. The relative importance of external heat transfer mechanisms in wildland fire has been a subject of debate for several decades and recent work has begun to demonstrate the importance of convective heating [12,13]. According to McAllister et al. [14], when thermal radiation alone was used as a heating mode, an addition pilot source was required to cause ignition. However, according to Pickett et al. [15], when the convective heating was used; achieved by subjecting the vegetation to hot gases, it caused ignition without the aid of a pilot. Preliminary results of a current study have shown that a thermal

* Corresponding author. Fax: +1 256 824 6758.
E-mail address: babak.shotorban@uah.edu (B. Shotorban).

http://dx.doi.org/10.1016/j.combustflame.2015.10.006
0010-2180/

Greek symbols

$\boldsymbol{\tau}$	stress tensor
χ_s	fraction of consumed fuel mass converted to soot
Δ	filter width
δ	cell size (m)
$\dot{\omega}'''$	volumetric source term (kg/m^3 s)
ϵ	emissivity
ν_α	reaction stoichiometric coefficients
ν_t	eddy viscosity (m^2/s)
ϕ	generic scalar
ψ	porosity
ρ	density (kg/m^3)
K	permeability (m^2)
ν	kinematic viscosity (m^2/s)

Variables

$\dot{Q}'''$	heat of reaction in the solid phase (W/m^3)
$\hat{\mathbf{s}}$	unit vector in the direction of radiation intensity
$\hat{\mathbf{x}}$	position vector (m)
Pr_t	turbulent Prandtl number
$\mathrm{R_u}$	universal gas constant (J/mole K)
Sc_t	turbulent Schmidt number
A	pre-exponential factor (1/s)
C_s	smagorinsky constant
c_p	specific heat capacity (J/kg K)
D	diffusivity (m^2/s)
E	activation energy (kJ/mol)
G	normalized filter kernel function
G_m	specific gravity of moist wood
h	sensible enthalpy (J/kg)
H_c	heat of combustion (J/kg)
h_c	heat transfer coefficient (W/m^2 K)
I	radiation intensity (W/m^2 sr)
k	thermal conductivity (W/m K)
M_c	fuel moisture content
M_s	number of solid phase reactions
n_α	number of species
P	background pressure (Pa)
p	perturbation pressure (Pa)
P_g	gas phase pressure within the solid fuel (Pa)
T	temperature (K)
t	time (s)
U	total radiation intensity in the gas phase (W/m^2)
W	molecular weight (kg/kmol)
x	distance (m)
Y	mass fraction
y	distance (m)
z	distance (m)
$\mathbf{J}$	diffusion flux of gas phase species (kg/m^2 s)
$\mathbf{J}_\alpha^g$	diffusion mass flux (kg/m^2 s)
$\mathbf{n}$	unit vector normal to the boundary surface
$\mathbf{S}$	strain rate tensor
$\mathbf{u}$	velocity vector (m/s)
$\dot{\mathbf{m}}''$	convective mass flux (kg/m^2 s)

Superscripts

∞	ambient (as in the solid–gas interface)
sgs	subgrid stress

Subscripts

α	solid/gas phase species
d	destruction
F	fuel species
f	formation
g	gas phase within the solid fuel
s	solid phase

radiation flux of 50 kW/m^2 will not ignite live fuels. Gallacher *et al.* [16] and Engstrom *et al.* [17] used a radiant panel with a maximum heat flux of 50 kW/m^2 as the heating source to study effects of radiative heating on the leaves of manzanita (Arctostaphylos glandulosa), oak (Quercus berberidifolia), ceanothus (Ceanothus crassifolius) and chamise (Adenostoma fasciculatum) species. They reported that no ignition or visible flame was observed when the radiation alone was the source of heating, so the radiant source was dropped from the experiment in order to determine the burning characteristics using the flat flame burner convective source. The experiments measured the surface and tip temperature history of the leaf using IR camera and type-K thermocouple respectively. Ignition criteria used in these experiments was based on a visible flame through a video data obtained at 30 frames per second using PCI 1411 (NI)DAQ card and Hi-8 camcorder.[1]

When a solid fuel is heated to a sufficiently high temperature, it undergoes thermal degradation [18]. For the purpose of modeling, thermal degradation is assumed to occur in two sequential steps. The first step is pyrolysis, which is usually an endothermic process that breaks down vegetation composed of cellulose, hemicelluloses, and lignin into low molecular mass gases (pyrolyzates), tars, carbonaceous char and mineral ash. The second step is combustion wherein the gases are ignited and oxidized resulting in a visible diffusion flame. Ignition criteria have been defined for solid phase, the gas phase or combined solid and gas phases [19]. In the present study, we defined ignition based on the gas phase. Critical mass flux and heat release rate (HRR) define ignition. A single value of heat release rate, as a reasonable criterion for ignition, has been proposed [20,21]. We defined ignition as the time at which the HRR exceeded 200 kW/m^3 in the gas phase over the surface of cellulose element. Any value above this critical value would mean an active flame observed in the simulation over the solid fuel.

The solid fuel (vegetation) consists of different polymers present in the organic fraction of the fuel and the mass of the inorganic fraction is generally very low in most fuels ($<$ 5%). Hemicellulose, cellulose and lignin comprise 20–40%, 40–60%, and 10–25% of biomass, respectively [2,22,23] with cellulose being the main component [22]. The interest in modeling fire and using biomass as an energy fuel has resulted in a large body of work characterizing biomass fuels and their thermal degradation over the past 60 years [18, 24–27]. Chemical reactions of cellulosic materials exposed to high temperature sources can be broadly classified as primary and secondary reactions. Primary reactions are concerned with the degradation of the cellulosic fuel into char and numerous volatile products whereas secondary reactions are those undergone by primary volatile products [28]. The first kinetic models were proposed in the 1960s by Kilzer and Broido [29], Chatterjee and Conrad [30] and Shafizadeh [31], and form the basis of more recent kinetic models. Cellulose is assumed to decompose through two parallel or competitive reactions [29,31]. Results obtained by Broido [29] and other investigators [30,31] indicated that lower heating rates yield more char. Below approximately 280 °C, the formation of char is assumed favored while above this temperature, formation of tar is assumed favored. The reason for this assumption could be due to the predominant depolymerization reactions associated to the breakage of glycosidic bonds [32].

[1] The use of trade or firm names in this publication is for reader information and does not imply endorsement by the U.S. Department of Agriculture of any product or service.

For high heating rates (4000–10, 000 °C/s), Lewellen et al. [33] suggested that there is no char formation and liquid tar is produced instead. Several investigators have developed multi-step kinetic models derived from the original mechanism of Kilzer and Broido [29]. Bradbury et al. [34] reformulated Broido's reaction model by introducing active cellulose, as an intermediate species between native cellulose and reaction products and this reaction model is called as 'Broido–Shafizadeh model (BS)'. The 'extended Broido–Shafizadeh model' [35] was developed by Blasi [28] who used the BS model and extended it to include secondary reactions for tar cracking.

Water present in vegetation is an important factor that influences the burning behavior of live fuels [36] and vegetation flammability has been associated with its moisture content (mass of water as a percentage of dry mass – FMC). However, recent work suggests that moisture content changes (and hence flammability) over a growing season in response to lack of precipitation are also due to changes in the biomass as a result of growth and other physiological processes [37]. Jolly et al. [37] demonstrated that changes to dry matter exert a stronger control on seasonal live fuel moisture content dynamics than actual changes in water content, and their results challenge the assumption that the fuel moisture content variations are strongly related to water stress. In addition to the water contained in living plants, water is also a product of pyrolysis and the combustion reaction [38]. When the oven-dry moisture content exceeds 56% in an idealized fuel, the amount of water released by evaporation exceeds the amount produced by combustion [39].

In a series of numerical experiments wherein water vapor was introduced into the gas mixture of an opposed flow flame and of a diffusion flame, water vapor diluted the mixture making it more difficult to generate a flammable mixture [40]. Ignition temperature of wood has been found to increase by about 2 °C for each percent increase in moisture [41]. Water has three effects on the solid phase [42]: it changes the thermal properties of the material (density, thermal conductivity, and specific heat), it transfers heat by molecular diffusion, and its evaporation is strongly endothermic. Some disagreement is evident in the literature about whether FMC has a stronger effect on the solid phase or the gas phase. Babrauskas [19] states the gas phase effect to be minor in comparison to the solid phase effects. Moreover, temperature profiles and pyrolysis rates at different points are modified by the FMC. However, Abu-Zaid [43] claims that the increase in ignition temperature with FMC is more important than the impact on solid pyrolysis. Pickett et al. [15] investigated the burning of various live leaf samples in detail and reported that ignition did not occur at the end of global evaporation, as predicted by conventional models, but possibly at the end of local evaporation. They also found that a significant amount of moisture (30–60%) remained in the sample for most species at the time of ignition. The experiments did not focus on pyrolysis and other physical processes inside the fuel. Experiments conducted by McAllister et al. [14] also reported significant temperature and moisture gradients inside the solid during pyrolysis of live foliar fuels which have been assumed to be thermally thin. The research work so far in the context of live fuels [14–16] has been successful in describing the burning characteristics of individual live leaf samples in terms of temperature at which moisture is released, ignition time depending on the species FMC and burnout times. However, there is a dearth of information regarding how the constituents of these species are structurally and chemically different from other species [44] and even less information on how moisture is distributed within them. To the best of our knowledge, behavior of moisture in the context of wood has been well established but in the context of live fuels, more investigation is required in order to accurately model the physical system. Considering such a limitation, our investigation focuses on main components such as cellulose and water, based on available literature of wood in order to facilitate computational modeling of an individual leaf-like fuel element.

The main aim of the present work is to better understand the effects of thermal radiation and moisture content on pyrolysis of solid fuel composed of cellulose and the subsequent gas phase ignition. This was accomplished by taking into account multi-step thermophysical processes occurring in the solid fuel and the associated combustion of the released gases using a three-dimensional solid-gas coupled model. The solid model used Gpyro3D [45] for pyrolysis and the gas phase fluid dynamics and combustion were solved using Fire Dynamics Simulator (FDS) [46,47]. Development and validation of this model is the first step in our effort to model the pyrolysis and ignition of live vegetation and compare the results to data from the FIST apparatus and a flat-flame burner with a radiant panel [14,16].

2. Mathematical and reaction models

Prior work has observed appreciable temperature and moisture variation on the surface of leaf fuel particles [15] and according to McAllister et al. [14] these gradients were observed along the depth of the fuel, indicating a three-dimensional nature of pyrolysis. CFD models such as FDS and FireFOAM divide the surface of three-dimensional objects into multiple one-dimensional "patches"; heat is transferred only in the direction normal to the surface of a patch, but not laterally in the directions parallel to the surface [45], which is important in the present context. Therefore, to investigate the three-dimensional effects during fire initiation and propagation on fuel elements where multidimensional heat and mass transfer effects are significant, a fully coupled Gpyro3D-FDS model is used. The solid phase model Gpyro3D has been coupled to the gas phase (FDS), at the interface by Lautenberger [45]. Detailed description of numerical approach, mathematical models used in Gpyro3D and FDS are given by Lautenberger [45] and McGrattan et al. [47], respectively. However an overview of governing equations in FDS (gas phase domain) and Gpyro3D (solid phase domain) outlining the variables involved during the coupling between solid-gas phase domain is presented here. Also, details of the existing and improved coupling method along with the pyrolysis model for cellulose are discussed.

2.1. Gas-phase equations

Large eddy simulation (LES) is used to deal with turbulence in this study. Given a generic field variable $f(\mathbf{x}, t)$, which is a function of position vector $\mathbf{x}$ and time t, LES is based on spatial filtering expressed as:

$$\bar{f}(\mathbf{x}, t) = \int f(\mathbf{x}', t) G(\mathbf{x}, \mathbf{x}'; \Delta) d\mathbf{x}' \tag{1}$$

where overbar denotes a spatially filtered quantity. Here G is a normalized filter kernel function, with Δ denoting the filter width and the integration is performed over the spatial domain. For compressible flows, it is more convenient to work with density-weighted or Favre filtered field (denoted by tilde) defined $\tilde{f}(\mathbf{x}, t) = \overline{\rho f}/\bar{\rho}$.

The filtered equations of FDS are presented below followed by formulations for combustion chemistry, thermal radiation and convective heat transfer. Further details of the gas phase equations, including the numerical approach, discretization and boundary condition implementation can be found in [47]. The Favre-filtered transport equations for mass, species, momentum and enthalpy, combined with the equation of state (EOS), shown below in Eqs. (2)–(6), provide $n_\alpha + 5$ independent equations (n_α is the number of species) for $n_\alpha + 5$ unknowns including density, $n_\alpha - 1$ mass fractions, 3 velocity components, hydrodynamic pressure, and enthalpy:

$$\frac{\partial \bar{\rho}}{\partial t} + \nabla \cdot (\bar{\rho} \tilde{\mathbf{u}}) = 0, \tag{2}$$

Table 1
Constitutive relations and subgrid models. The eddy viscosity is obtained from the constant coefficient Smagorinsky model, $\nu_t = (C_s\Delta)^2|\tilde{\mathbf{S}}|$ with $C_s = 0.2$ and $\Delta = \delta$. The magnitude of the strain rate is $|\tilde{\mathbf{S}}| = (2\tilde{\mathbf{S}} : \tilde{\mathbf{S}})^{1/2}$. The turbulent Schmidt and Prandtl numbers are assumed as $\mathrm{Sc}_t = 0.5$ and $\mathrm{Pr}_t = 0.5$, respectively.

Species flux	$\left(\bar{\mathbf{J}}_\alpha + \mathbf{J}_\alpha^{\mathrm{sgs}}\right) = -\bar{\rho}(\tilde{D}_\alpha + \frac{\nu_t}{\mathrm{Sc}_t})\nabla\tilde{Y}_\alpha$
Momentum flux	$\bar{\boldsymbol{\tau}} = -2\bar{\mu}\left(\tilde{\mathbf{S}} - \frac{1}{3}(\nabla\cdot\tilde{\mathbf{u}})\mathbf{I}\right)$
	$\boldsymbol{\tau}^{\mathrm{sgs,d}} \equiv \boldsymbol{\tau}^{\mathrm{sgs}} - \frac{1}{3}\mathrm{trace}(\boldsymbol{\tau}^{\mathrm{sgs}})$
	$= -2\bar{\rho}\tilde{\nu}_t\left(\tilde{\mathbf{S}} - \frac{1}{3}(\nabla\cdot\tilde{\mathbf{u}})\mathbf{I}\right)$
Heat flux	$(\bar{\mathbf{q}} + \mathbf{q}^{\mathrm{sgs}}) = -(\tilde{k} + \bar{\rho}\tilde{c}_p\frac{\nu_t}{\mathrm{Pr}_t})\nabla\tilde{T}$

Table 2
Summary of source terms: The combustion model is based on mixing time τ (see Section 2.1). In the radiation source term I represents the emission term based on filtered temperature of the gas or temperature of the solid fuel. The term U represents the integrated radiation intensity. Detailed description about the formulation of these terms could be found in [47].

Chemical source term	$\overline{\dot{m}_F'''} = -\frac{\min(\bar{\rho}\tilde{Y}_F, \bar{\rho}\tilde{Y}_{O_2}, r_{O_2})}{\tau}$
Radiation and diffusion source terms	$\bar{\mathbf{q}}_{\mathrm{d}} = -\sum_\alpha \bar{\rho}D_\alpha\tilde{h}_\alpha\nabla\tilde{Y}_\alpha$
	$\overline{\dot{q}_{\mathrm{r}}'''} = \kappa[4\pi I_b(\tilde{T}) - \bar{U}]$

$$\frac{\partial\bar{\rho}\tilde{Y}_\alpha}{\partial t} + \nabla\cdot\left(\bar{\rho}\tilde{\mathbf{u}}\tilde{Y}_\alpha\right) = -\nabla\cdot\left(\bar{\mathbf{J}}_\alpha + \mathbf{J}_\alpha^{\mathrm{sgs}}\right) + \overline{\dot{m}_\alpha'''}, \tag{3}$$

$$\frac{\partial\bar{\rho}\tilde{\mathbf{u}}}{\partial t} + \nabla\cdot(\bar{\rho}\tilde{\mathbf{u}}\tilde{\mathbf{u}}) = -\nabla\bar{p} - \nabla\cdot(\bar{\boldsymbol{\tau}} + \boldsymbol{\tau}^{\mathrm{sgs}}) + \bar{\rho}\mathbf{g}, \tag{4}$$

$$\frac{\partial\bar{\rho}\tilde{h}}{\partial t} + \nabla.(\bar{\rho}\tilde{\mathbf{u}}\tilde{h}) = \frac{D\bar{P}}{Dt} - \nabla\cdot(\bar{\mathbf{q}} + \mathbf{q}^{\mathrm{sgs}} + \bar{\mathbf{q}}_{\mathrm{d}}) + \overline{\dot{q}'''} - \overline{\dot{q}_{\mathrm{r}}'''}, \tag{5}$$

$$\bar{P} = \bar{\rho}\mathrm{R_u}\tilde{T}\sum_{\alpha=1}^{n_\alpha}\frac{\tilde{Y}_\alpha}{W_\alpha}, \tag{6}$$

In the above set of equations, $\bar{\rho}$ is the filtered gas mixture density, $\tilde{\mathbf{u}}$ denotes the Favre-filtered velocity vector, $\bar{P}$ is the background pressure, $\bar{P}$ is the perturbation pressure, $\tilde{T}$ is the filtered gas phase temperature, and $\mathrm{R_u}$ is the universal gas constant. In the filtered species conservation Eq. (3), $\tilde{Y}_\alpha$ is the mass fraction of the gas-phase species α, $\overline{\dot{m}_\alpha'''}$ is the chemical source term due to combustion, and $\bar{\mathbf{J}}_\alpha$ and $\mathbf{J}_\alpha^{\mathrm{sgs}}$ represent the molecular species diffusion flux and subgrid-scale (SGS) species diffusion flux, respectively. In the momentum Eq. (4), and $\bar{\boldsymbol{\tau}}$ and $\boldsymbol{\tau}^{\mathrm{sgs}}$ represent viscous and SGS stress tensors, respectively. In the energy Eq. (5), $\tilde{h}$ is the sensible enthalpy of the gas mixture, $\bar{\mathbf{q}}$, $\mathbf{q}^{\mathrm{sgs}}$ and $\bar{\mathbf{q}}_{\mathrm{d}}$ represent the conductive, SGS heat and diffusive fluxes, respectively, $\overline{\dot{q}'''}$ denotes the source term due to heat release during combustion, and $\overline{\dot{q}_{\mathrm{r}}'''}$ accounts for the radiation. All the formulations pertaining to flux and source terms are given in Tables 1 and 2 respectively. Eqs. (2)–(5) are solved using a Predictor–Corrector method. First the thermodynamic variables $\bar{\rho}$, $\tilde{Y}_\alpha$ and $\bar{P}$ are computed, followed by calculation of velocity divergence in the predictor step which is then used as a constraint to solve the Poisson equation for the hydrodynamic pressure in the correction step. The convective fluxes are computed using second order TVD schemes such as Superbee and the spatial and temporal discretization is second order accurate. Calculation of the time step is based on satisfying stability criteria dictated by Courant number, which is based on the cell face convective velocities.

The chemical source term for fuel $\overline{\dot{m}_F'''}$ is modeled using the Eddy Dissipation Concept (EDC) [48]. The equation for this term is given in Table 2 where τ is the mixing time and calculated in this work through a procedure similar to what McGrattan et al. [49] propose. Three physical processes of diffusion, subgrid-scale turbulent diffusion and buoyant acceleration are taken into account and the mixing time is calculated locally based on the fastest of them as the controlling time scale: $\tau = \min(\tau_d, \tau_u, \tau_g)$ where $\tau_d = \Delta^2/D_F$, $\tau_u = C_{\mathrm{EDC}}\Delta^2\mathrm{Sc_t}/\nu_t$ [50] and $\tau_g = \sqrt{2\Delta/g}$, are time scales associated with diffusion, subgrid-scale turbulent diffusion, and buoyant acceleration, respectively. Here, D_F is the fuel molecular diffusion, and C_{EDC} is a model constant set to 0.1 [50].

2.1.1. Chemical reactions

The molar heat of combustion for a given chemical reaction at constant pressure is [51,52]

$$\Delta H_c = -\sum_\alpha \nu_\alpha h_\alpha(T)W_\alpha \tag{7}$$

where $\nu_\alpha, h_\alpha, W_\alpha$ are the stiochiometric coefficient, total enthalpy and molecular weight of the gas species α, respectively. The simplified stiochiometric relation

$$\mathrm{CH_4} + 2(\mathrm{O_2} + 3.76\mathrm{N_2}) \rightarrow \mathrm{CO_2} + 2\mathrm{H_2O} + 7.52\mathrm{N_2} \tag{8}$$

is used to model the chemical reaction between air and fuel vapor generated by solid pyrolysis, where the latter is modeled as methane. It is noted that the main pyrolysis gases produced by cellulose contain carbon dioxide, carbon monoxide and hydrogen in addition to methane. It was indicated by Yang et al. [22] that methane is a main gas product during the pyrolysis of cellulose, hemicellulose and lignin. Following the work by Dahale et al. [53], who used methane as a surrogate fuel for the modeling of wildland fires, here we also used methane as a surrogate to facilitate the modeling.

The heat release rate (HRR) per unit volume of the combustion process can be represented in terms of heat of combustion,

$$\overline{\dot{q}'''} = -\overline{\dot{m}_F'''}\Delta\tilde{h}_c \tag{9}$$

where $\Delta\tilde{h}_c = \Delta H_c/W_F$ is the mass-based heat of combustion evaluated at $\tilde{T}$. The efficiency of combustion calculated during the simulation was in the range of 60–70% at peak HRR.

2.1.2. Thermal radiation transport

The net contribution from thermal radiation in the energy equation of the gas phase is defined by the radiation transport equation (RTE):

$$\hat{\mathbf{s}}\cdot\nabla\bar{I}(\mathbf{x},\hat{\mathbf{s}}) = \kappa[I_b(\tilde{T}) - \bar{I}(\mathbf{x},\hat{\mathbf{s}})] \tag{10}$$

where $I(\mathbf{x})$ is the solution of the RTE, $I_b(\mathbf{x})$ is the emission source term evaluated using the filtered temperature field $\tilde{T}$ [47] and $\kappa(\mathbf{x})$ is the absorption coefficient. The absorption coefficients are obtained for various species during the chemical reaction and soot using a narrow-band model called RadCal [54]. Here we have invoked the grey gas assumption, which is appropriate for fires from vegetative fuels [55]. Soot evolution model is not used, instead the mass of soot generated is based on an assumed fraction, χ_s, of the mass of fuel gas consumed by the combustion reaction. The value assumed for χ_s is 0.01 based on data available for Douglas fir ranging from less than 0.01 to 0.025 under flaming conditions [56]. The number of solid angles used here was 104. Integrating the RTE (10) over all the solid angles gives the equation for conservation of radiant energy.

$$\overline{\dot{q}_{\mathrm{r}}'''}(\mathbf{x}) = \kappa[4\pi I_b(\tilde{T}) - \bar{U}(\mathbf{x})] \tag{11}$$

where $\bar{U}$ is the integrated radiation intensity. The radiation equation is solved using a finite volume method based on Raithby and Chui [57]. The finite volume solver requires about 20% of the total CPU time of a calculation, a modest cost given the complexity of radiation heat transfer.

2.1.3. Convective heat transfer

In the LES calculation, convective heat flux to the surface of the solid fuel is obtained from a combination of natural and forced convection correlations

$$h = \max\left[C|T_g - T_s|^{\frac{1}{3}}, \frac{k_g}{L}(0.0037)\mathrm{Re}^{\frac{4}{5}}\mathrm{Pr}^{\frac{1}{3}}\right] \ \mathrm{W/m^2\,K} \tag{12}$$

where C is the coefficient for natural convection (1.52 for a horizontally oriented solid fuel) [58], L is a characteristic length related to the size of the solid fuel used, k_g is the thermal conductivity of the gas, and the Reynolds Re and Prandtl Pr numbers are based on the gas flowing past the obstruction. The convective heat flux calculation is based on the formulation given in Table 2.

2.2. Solid-phase equations

The three-dimensional porous media conservation equations for mass, species, momentum and energy in Gpyro3D, the solid fuel model, are presented below in Eqs. (13)–(18). The following assumptions are inherent to this model:

- Each solid phase species α has well-defined properties that are temperature dependent: bulk density (ρ_α), specific heat capacity ($c_{p\alpha}$), effective thermal conductivity (k_α), emissivity (ϵ_α), permeability (K_α), porosity (ψ_α).
- Radiation heat transfer across pores is not accounted for and only surface absorption of radiation is considered.
- All gaseous species within the solid fuel have equal diffusion coefficient, D (independent of temperature).
- Darcian pressure-driven flow through porous media (Stokes flow).
- Unity Schmidt number, hence $\nu = D$.
- Gas phase and solid phase are in thermal equilibrium ($T_g = T_s$).
- No shrinkage or swelling (volume change) occurs.

$$\frac{\partial \rho_s}{\partial t} = -\dot{\omega}'''_{fg}, \tag{13}$$

$$\frac{\partial \rho_s Y^s_\alpha}{\partial t} = \dot{\omega}'''_{fs\alpha} - \dot{\omega}'''_{ds\alpha}, \tag{14}$$

$$\frac{\partial (\rho_s h_s)}{\partial t} = -\nabla \cdot \mathbf{q}_s - \dot{Q}'''_{s-g} + \sum_{\alpha=1}^{M_s} (\dot{\omega}'''_{fs\alpha} - \dot{\omega}'''_{ds\alpha}) h_\alpha \tag{15}$$

$$\frac{\partial \rho_g \psi}{\partial t} + \nabla \cdot \dot{\mathbf{m}}'' = \dot{\omega}'''_{fg} \tag{16}$$

$$\frac{\partial \rho_g \psi Y^g_\alpha}{\partial t} + \nabla \cdot \left(Y^g_\alpha \dot{\mathbf{m}}''\right) = -\nabla \cdot \mathbf{J}^g_\alpha + \dot{\omega}'''_{fg\alpha} - \dot{\omega}'''_{dg\alpha} \tag{17}$$

where

$$\mathbf{q}_s = -k \nabla T_s, \quad \dot{\mathbf{m}}'' = -\frac{K}{\nu} \nabla P_g, \quad \mathbf{J}^g_\alpha = -\psi \rho_g D \nabla Y^g_\alpha. \tag{18}$$

The solid phase mass, species and energy conservation are given in Eqs. (13)–(15). Similarly mass, and species conservation for the gas phase present within the solid fuel are presented in Eqs. (16)–(17). In these equations, ρ_s, h_s, ψ, K, k denotes weighted quantities i.e. $k = \sum X_\alpha k_\alpha$. Subscripts s, g, α, f, d denote solid phase, gas phase within the solid fuel, solid/gas-phase species within the solid fuel, formation and destruction, respectively. Eq. (16) of the mass conservation of gas species is not explicitly solved, but it is used to form a pressure evolution equation through the ideal gas law for the gas phase density ρ_g and Darcy's law for the convective mass flux $\dot{\mathbf{m}}''$ as shown in Eq. (18). The diffusion coefficient D in Eq. (18) is calculated from Chapman–Enskog theory [59]. In Eq. (18), ν is the kinematic viscosity of gas species. The term $\dot{\omega}'''$ represents volumetric source term for formation or destruction of species and $\dot{Q}'''$ represents the volumetric source term for heat generated or absorbed during any reaction. The details on the formulations of the source terms are given in [45].

When discretized, the above equations yield a system of coupled algebraic equations that are solved numerically. Due to the nonlinearity introduced by the source terms and temperature-dependent thermophysical properties, a fully-implicit formulation is adopted for the solution of all equations. The condensed phase energy conservation equation, gas phase species conservation equation, and gas phase momentum conservation equation are solved using the Tridiagonal Matrix Algorithm [60]. The solid fuel mass and species conservation equations are solved with a customized fully implicit solver that uses relaxation to prevent divergence.

Table 3
Initial mass fractions of solid and gas species within the solid fuel.

FMC (%)	Moisture	Cellulose	N_2	O_2
80	0.46	0.54	0.77	0.23
40	0.22	0.78	0.77	0.23
5	0.04	0.96	0.77	0.23

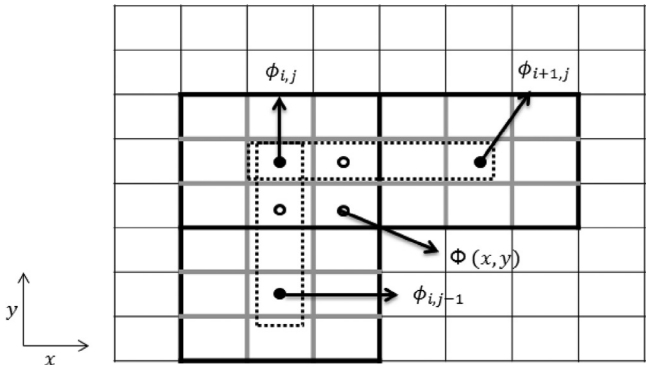

Fig. 1. Schematic representing bilinear interpolation used to couple the solid fuel domain solver variables to gas-phase solver variables; top view of xy-slice at the interface of solid fuel and gas-phase domain.

Initially, the solid-phase domain in Gpyro3D consists of the solid phase species including moisture and cellulose, and the gas phase species including nitrogen and oxygen with initial mass fractions given in Table 3. The initial temperature and ambient pressure are 300 K and 101.3 kPa, respectively. Gpyro3D (solid fuel domain) is coupled to FDS (gas phase domain) by obtaining the temperature, total radiation intensity, species mass fractions and convective heat transfer coefficient from FDS, which are applied as boundary conditions to the solid phase. The following equation is used as the boundary condition for the solid phase energy Eq. (15):

$$k \nabla T_s \cdot \mathbf{n} = \bar{\epsilon} \bar{U} - \bar{\epsilon} \sigma T_s^4 - h_c \left(T_s - \tilde{T}_\infty\right) \tag{19}$$

where quantities h_c, $\tilde{T}_\infty$, $\bar{U}$ that represent heat transfer coefficient, ambient fluid temperature, and total radiation intensity are obtained from the gas phase domain (FDS domain) external to the solid fuel. No boundary conditions are needed for the mass or solid phase species conservation equations since there are no convective or diffusive terms in Eqs. (13) and (14). The gas phase species conservation Eq. (17) uses the following equation:

$$\dot{\mathbf{m}}''_\alpha \cdot \mathbf{n} - Y^g_\alpha \dot{\mathbf{m}}'' \cdot \mathbf{n} = \frac{h_c}{c_{pg}} \left(Y^g_\alpha - \tilde{Y}^\infty_\alpha\right) \tag{20}$$

where $\dot{\mathbf{m}}''_\alpha$ is the total mass flux of species α, $\dot{\mathbf{m}}''$ is given in Eq. (18) and $\tilde{Y}^\infty_\alpha$ represents the ambient mass fraction of the species α given by FDS.

In the existing coupling method, a solid fuel cell in Gpyro3D at the interface communicates with the closest gas phase cell in the FDS domain. This communication is schematically shown in Fig. 1. In this figure, filled circles represent the centers of FDS cells shown by rectangles with dark lines. Open circles represent the centers of Gpyro3D cells shown by gray lines. Here, ϕ is a generic variable, e.g., a particular species, of the FDS domain. Indices i and j represent the cell index of the FDS cell in x and y directions, respectively. Consider Φ to represent the interpolated value of the same variable in Gpyro3D. Here, a bilinear interpolation scheme is employed at the interface of solid

Table 4
Kinetic data pertaining to 5-step reaction model in the solid fuel.

Reaction	$A(s^{-1})$	E(kJ/mol)	Δh(kJ/kg)
R1	5.13×10^{10}	88	44
R2	2.8×10^{19}	242.4	0
R3	1.3×10^{10}	150.5	418
R4	3.28×10^{14}	196.5	418
R5	4.28×10^{6}	108	−42

fuel and surrounding gas phase:

$$\Phi(x,y) = \phi_{i,j} + \frac{\phi_{i,j} - \phi_{i+1,j}}{x_i - x_{i+1}}(x_i - x) + \frac{\phi_{i,j} - \phi_{i,j-1}}{y_j - y_{j-1}}(y_j - y). \quad (21)$$

The above interpolation scheme was utilized at all interfaces of the solid fuel and gas-phase domains. After the needed variables are passed from FDS to Gpyro3D, the solution is advanced for one time step for the solid fuel domain. The obtained temperature, convective heat flux, species, and species mass fluxes at the interface are then communicated from Gpyro3D to FDS. Then the FDS solver is advanced in time for one time step.

2.2.1. Chemical reactions

The chemical reactions included in the solid phase to model pyrolysis are as follows:

$$\text{Moisture (s)} \longrightarrow \text{Water vapor (g)} \quad (R1)$$

$$\text{Cellulose (s)} \longrightarrow \text{Active cellulose (s)} \quad (R2)$$

$$\text{Active cellulose (s)} \longrightarrow \text{Char (s)} + \text{Fuel vapors (g)} \quad (R3)$$

$$\text{Active cellulose (s)} \longrightarrow \text{Tar (g)} \quad (R4)$$

$$\text{Tar (g)} + O_2\text{ (g)} \longrightarrow \text{Fuel vapors (g)} \quad (R5)$$

Reactions R2–R4, [34], are primary reactions and R5 [28] is a secondary reaction for pyrolysis of cellulose. The primary reactions are concerned with the breakdown of cellulose to lower molecular weight gases while the secondary reaction, which is an oxidation reaction, is concerned with the tar breakdown to low molecular weight gases. In the current study, reaction R1 and the thermophysical properties pertaining to it are included to investigate the effects of FMC [61]. For reactions R2–R5, they are adopted from [28]. The kinetic parameters and thermophysical properties for the above set of equation are given in Tables 4 and 5 respectively.

2.2.2. Thermophysical properties

Correlations for wood were used in this work due to a lack of correlations for cellulose. As discussed in Section 1, FMC affects the thermal properties of the material which we modeled as follows. Fiber saturation point (FSP) of most woods ranges from 30–40% (dry basis) which is equivalent to 23–29% (wet basis) [37,62]. Above FSP, all the water in the plant cell lumen existed as free state. Below FSP, as FMC increased, both the density and volume increased until FSP is reached; above FSP, only density increased. For all FMC, Eq. (22) described the relationship between density and FMC [62]. Thermal conductivity and specific heat capacity were considered moisture dependent only when FMC was below FSP using Eqs. (26) and (27) from [62]. Eqs. (23) and (24) are used for the conductivity and heat capacity, respectively, when FMC = 0. The correlation in Eq. 26 given in [62], which includes the moisture content through dependency on FMC has

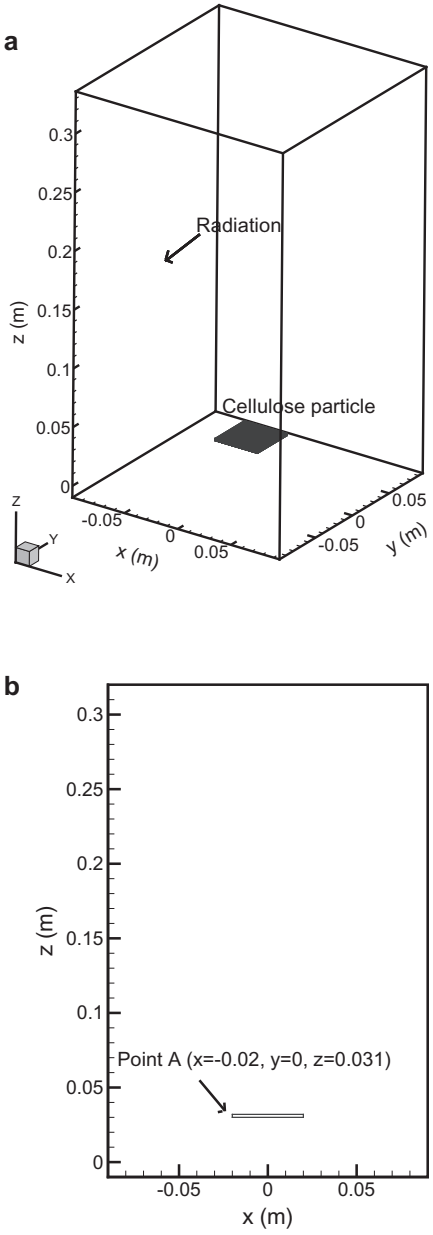

Fig. 2. (a) Isometric view of computational domain showing thin cellulose particle subjected to radiative heating from surface at $x = -0.09$ m and (b) two-dimensional view of computational domain along the xz-slice at $y = 0$. Point A located at $x = -0.02$ m, $y = 0$, $z = 0.031$ m is considered for analysis.

Table 5
Thermophysical properties pertaining to 5-step reaction model in the solid fuel.

Species	Molecular weight (g)	Density (kg/m^3)	Thermal conductivity (W/mK)	Specific heat (kJ/kg K)	Source
Moisture	–	1000	0.596	4.2	[61]
Cellulose	–	420	0.24	2.3	[70],[28]
Active cellulose	–	420	0.24	2.3	[70],[28]
Char	–	73	0.1	1.1	[70],[28]
Gases and tar	28	–	0.025	1.005	Assumed (Air)

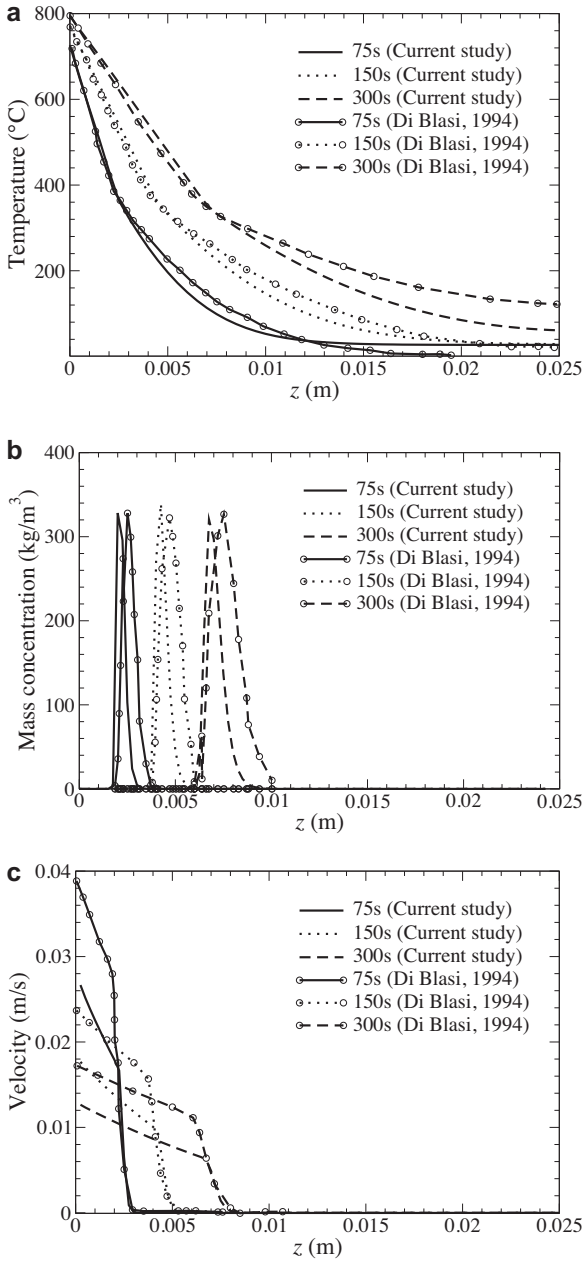

Fig. 3. Verification of results of current study using Gpyro for cellulose pyrolysis with simulations of Blasi [28] along the length of the specimen at different times; (a) temperature, (b) mass concentration of active cellulose and (c) velocity of gas species.

been proposed for temperature 24 °C. It is noted that the value of conductivity calculated by setting FMC = 0 in this correlation slightly differs from the value obtained through Eq. (23) for 24 °C. These thermophysical property correlations were used for the solid species for all the simulations invoking the coupled solver at various FMC cases (5%, 40% and 80%). The properties for the gas species were assumed from the available data for air.

$$\rho_{\text{cellulose}} = 1000\, G_m \left(1 + \frac{M_c}{100}\right) \quad (\text{kg m}^{-3}), \tag{22}$$

$$k_{\text{cellulose}-d} = 0.08124 + 0.003695\, T \quad (\text{W m}^{-1}\,\text{K}^{-1}), \tag{23}$$

$$c_{\text{cellulose}-d} = 0.1031 + 0.00386\, T \quad (\text{kJ kg}^{-1}\,\text{K}^{-1}), \tag{24}$$

$$A = (2.31 \times 10^{-4}\, T - 1.33 \times 10^{-4}\, M_c - 0.06191)\, M_c \tag{25}$$

$$k_{\text{cellulose}-m} = G_m\,(0.1941 + 0.004064\, M_c) + 0.01864 \quad (\text{W m}^{-1}\,\text{K}^{-1}), \tag{26}$$

$$c_{\text{cellulose}-m} = (c_{\text{cellulose}-d} + 0.0491\, M_c)/(1 + 0.01\, M_c) + A \quad (\text{kJ kg}^{-1}\,\text{K}^{-1}), \tag{27}$$

$$c_{\text{char}} = 1.39 + 0.00036\, T \quad (\text{kJ kg}^{-1}\,\text{K}^{-1}), \tag{28}$$

where ρ, G_m, M_c, k, T and c represent density, specific gravity, FMC, thermal conductivity, temperature and specific heat, respectively.

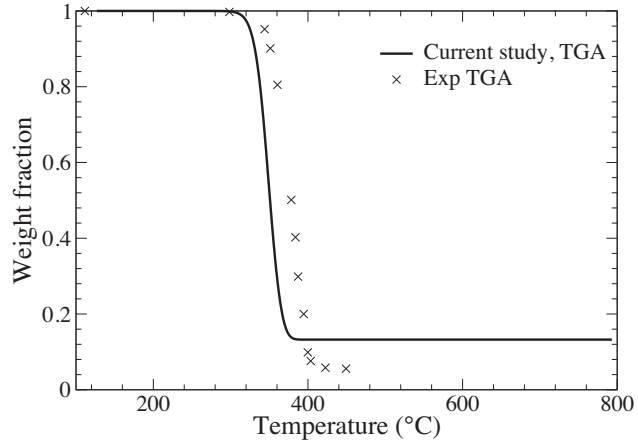

Fig. 4. Verification of results of current study using Gpyro TGA setup (solid line) with experimental TGA data [68] (crossmarks).

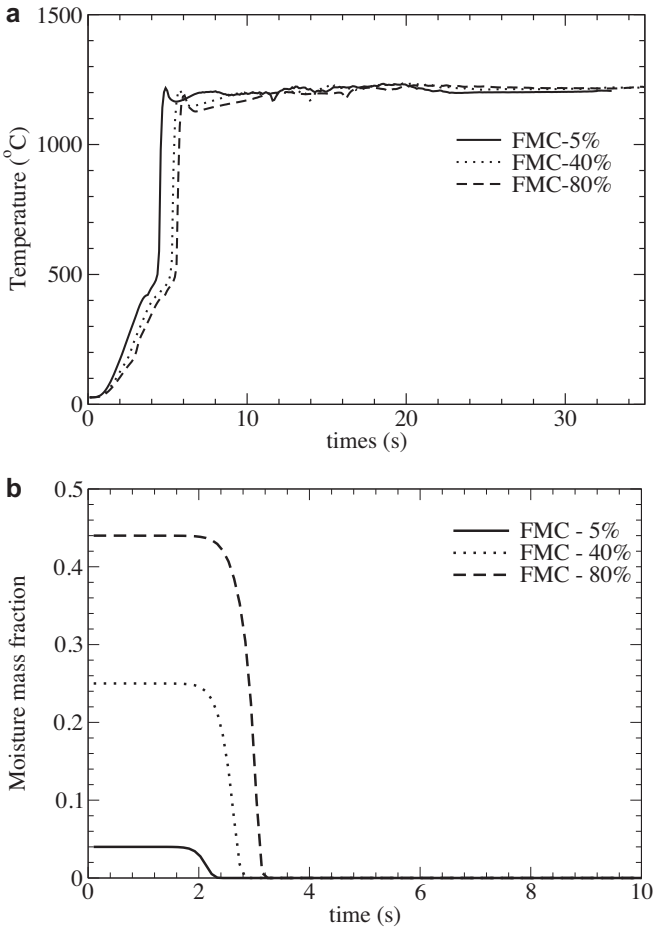

Fig. 5. Time history of (a) temperature, and (b) mass fraction of moisture at point A (see Fig. 2) for three cases with an initial FMC of 5%, 40% and 80%.

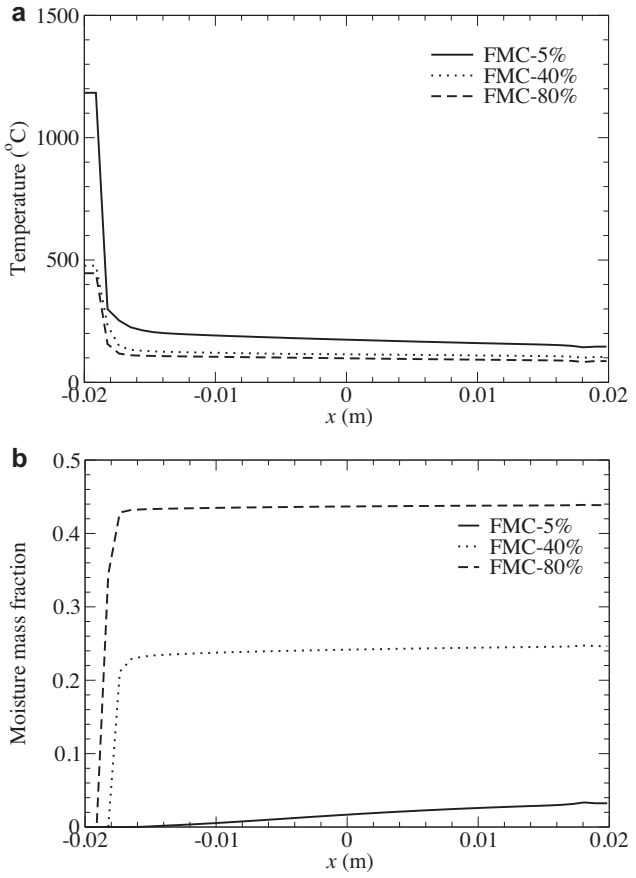

Fig. 6. Variation of (a) temperature and (b) mass fraction of moisture along x at $y = 0$ and $z = 0.031$ m at time 5 s in the solid phase for three cases with an initial FMC of 5%, 40% and 80%.

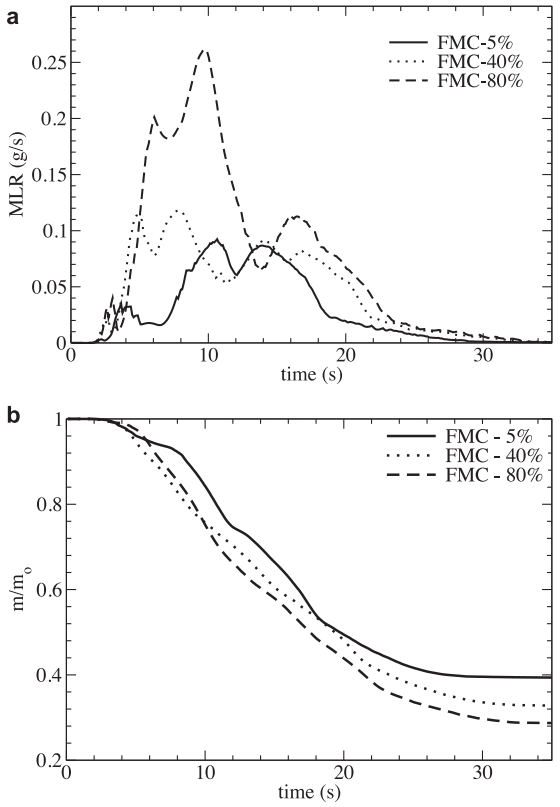

Fig. 7. Time history of (a) mass loss rate and (b) normalized mass in the solid phase for three cases with an initial FMC of 5%, 40% and 80%.

Subscripts m and d represent moist and dry conditions. The specific gravity was based on softwood species [62]. The properties for the remaining solid species were considered constant.

3. Physical configuration

The radiant heat fluxes associated with crown fires in conifers can be as high as 200 kW/m^2 [63]. The present work focused on the effect of FMC on ignition of a thin, rectangular piece of cellulose subjected to a radiant flux. A fuel element (0.04 × 0.04 × 0.002 m^3, L × W × T) of cellulose simulated the leaves studied by Pickett et al. [15] and Gallacher et al. [16]. The top surface of the solid fuel was located at $z = 0.032$ m and $y = 0$ was the leaf center line. Point A, a location in the domain within the fuel at which various quantities were graphed, was located at (−0.02, 0, 0.031). A schematic of the physical domain along with the boundary conditions is shown in Fig. 2. The computational domain used for the gas-phase solver FDS, was a rectangular cube of size $x = 0.18$ m, $y = 0.18$ m and $z = 0.32$ m. The grid resolution (x, y, z) in the gas phase was 72 × 72 × 92, respectively. The solid fuel particle was centered in the gas-phase domain and located at $z = 0.03$ m in the computational domain. The initial temperature, moisture content, pressure, gaseous species mass fractions, and condensed phase species were set uniform throughout the solid. The solid fuel element was simulated by Gpyro3D with a grid spacing of 0.0008 × 0.0008 × 0.0003 m^3 (x, y, z) resulting in 13,824 grid cells. There were 6 grid points along the thickness of the solid fuel. The fuel element was exposed to a radiant surface on one side located at $x = -0.09$ m and all the other sides had open boundary

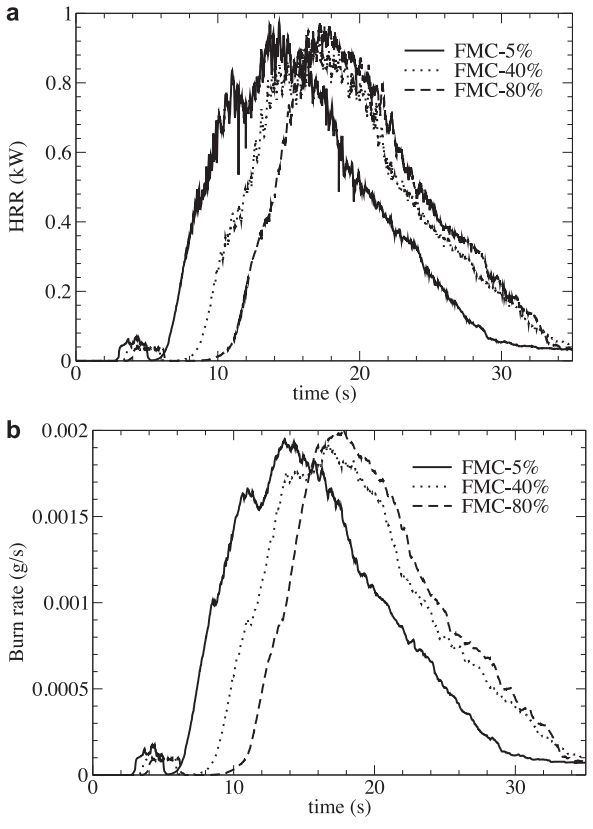

Fig. 8. Time history of (a) heat release rate and (b) burn rate in the gas phase for three cases with an initial FMC of 5%, 40% and 80%.

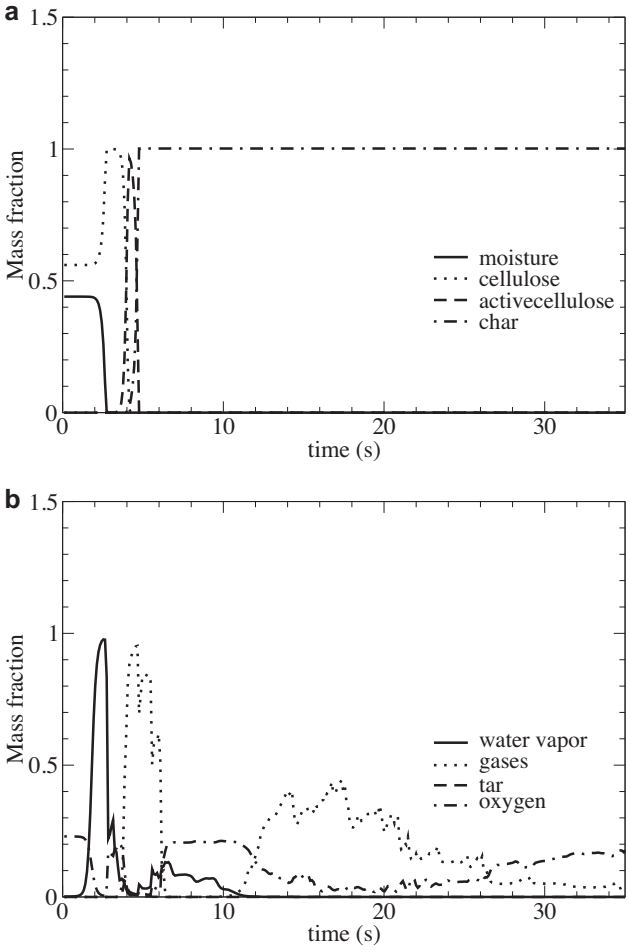

(b)

Fig. 9. Time history of (a) solid species and (b) gas species in the solid phase for a case with an initial FMC of 80% at point A.

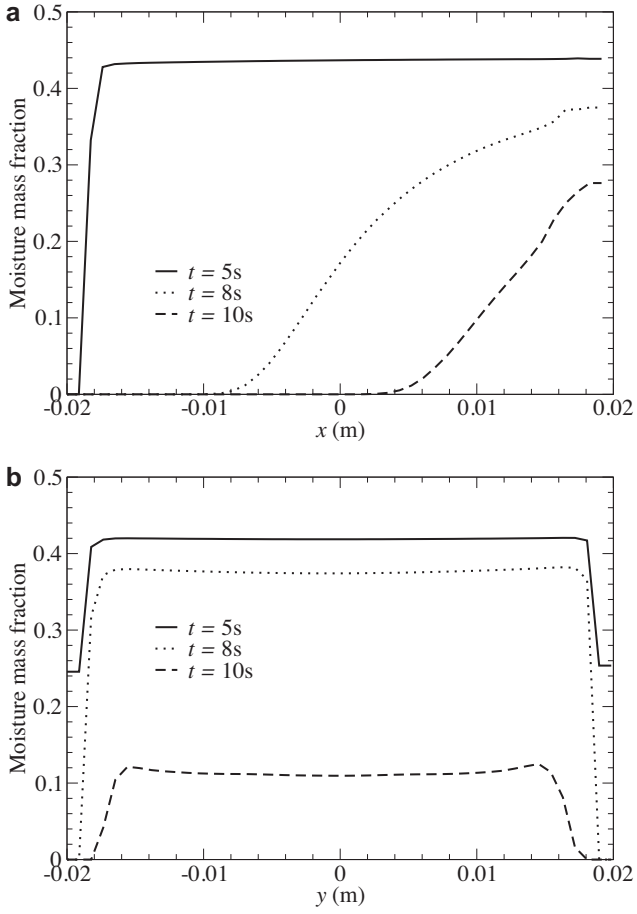

Fig. 10. Variation of moisture mass fraction (a) along x at $y = 0$ and $z = 0.031$ m and (b) along y at $x = 0.0125$ m and $z = 0.031$ m at various times in the solid phase for a case with an initial FMC of 80%.

conditions. The radiating surface was maintained at 1500 K during the simulation. All the computations were performed using Message Passing Interface (MPI) with 36 processors of Dense Memory Cluster (DMC) located at Alabama Supercomputer Authority. A typical simulation of 30 s required a wall time of 72 h and 64GB of memory.

4. Model verification and validation

In order to investigate the adequacy of this resolution, we also conducted simulations for a case with FMC of 80%, with two other resolutions, a higher resolution 120 × 120 × 160, and a lower resolution 48 × 48 × 64. The sensitivity of the results to the grid size was studied by comparing the heat release rates (HRR) calculated for three resolutions including the original one 72 × 72 × 96. The peak HRR value was found to increase by 10% as the grids were refined. This dependency of the results on the grid is believed to be inevitable due to the LES approach used in this work, which is based on spatial filtering (physical LES) [64]. In all the resolutions, we choose the grid size δ to be identical to the filter width Δ, i.e., $\Delta/\delta = 1$. This ratio is widely used in LES computations while it is acknowledged that it leads to less numerical accuracy, compared to the case simulated with the same δ but higher Δ. In other words, for an LES of fixed computational cost (fixed δ), the case with a larger value of Δ/δ will produce more numerically accurate results; however, a smaller range of turbulent motions will be resolved [64].

Another criterion for testing the grid resolution in fire modeling is based on the ratio $D^*/\delta x$, where D^* is a characteristic length scale of the fire obtained from the total heat release rate $\dot{Q}$ and ambient density, specific heat, and temperature and δx is the grid size has been found to be a convenient measure to determine the grid size in the FDS model [46]. Based on past numerical experiments, a ratio of 5–10 "usually produces favorable results at a moderate computational cost" [65].

$$D^* = \left(\frac{\dot{Q}}{\rho_o c_p T_o \sqrt{g}}\right)^{2/5} \tag{29}$$

In the present work, for the grid 72 × 72 × 92, the ratio $D^*/\delta x$ was about 15, which meets the criterion that the resolution that produces $\Delta^*/\delta > 10$ is adequate.

Another criterion to test the resolution is based on a quantity referred as measurement of turbulent resolution (MTR) has been investigated to assess the quality of the grid, 72 × 72 × 92 [46],

$$\mathrm{MTR}(\mathbf{x}, t) = \frac{k_{\mathrm{sgs}}}{k_{\mathrm{res}} + k_{\mathrm{sgs}}} \tag{30}$$

where

$$k_{\mathrm{res}} = \frac{1}{2}\tilde{u}\tilde{u} \tag{31}$$

$$k_{\mathrm{sgs}} = \frac{1}{2}(\tilde{u} - \hat{\tilde{u}})(\tilde{u} - \hat{\tilde{u}}) \tag{32}$$

Here, $\tilde{u}$ is the resolved filtered LES velocity and $\hat{\tilde{u}}$ is test filtered at a scale 2Δ. The time averaged values of MTR were found to lie between

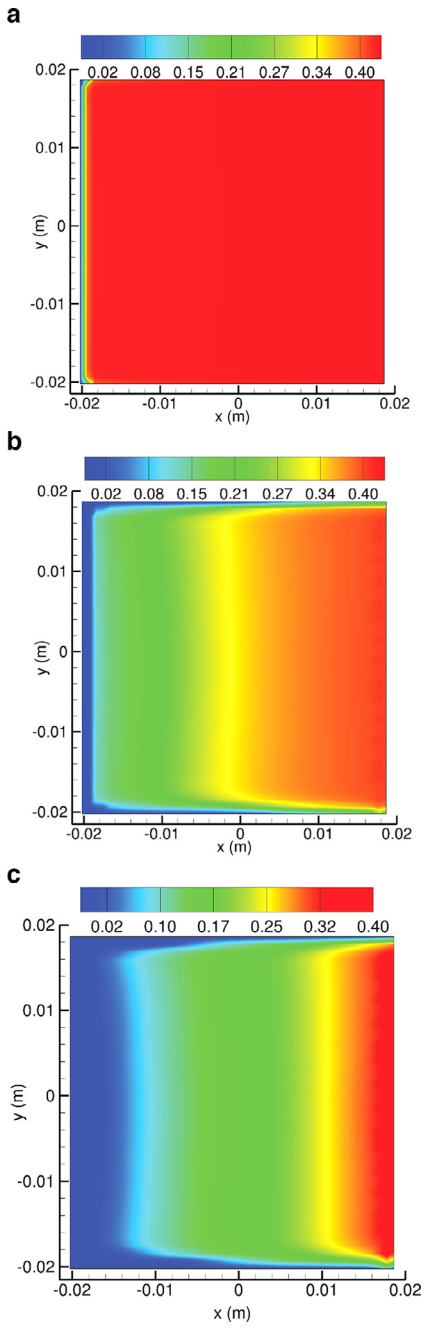

Fig. 11. Contours of moisture mass fraction in the solid fuel along x at (a) $t = 5$ s (b) $t = 6.5$ s and (c) $t = 7.75$ s on an xy-slice located at $z = 0.031$ m for a case with an initial FMC of 80%.

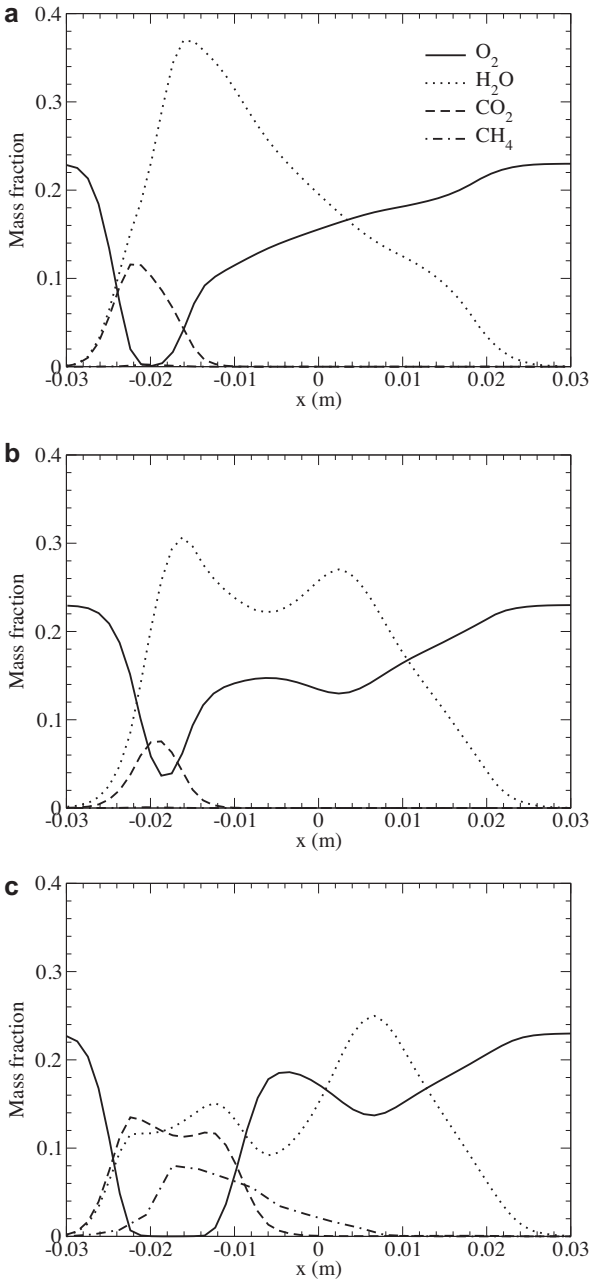

Fig. 12. Variation of mass fraction of tracked gas species at time (a) 5 s (b) 7.5 s and (c) 11 s along x at $y = 0$ and $z = 0.035$ m in the gas phase domain for a case with an initial FMC of 80%.

0.25–0.4 indicating that 60–80% of the kinetic energy was being resolved in the flow using this resolution.

Prior to simulating the effects of FMC and radiation on pyrolysis and ignition in the configuration described in Section 3, we performed verification and validation. Most bench-scale pyrolysis experiments that have been conducted to date are essentially designed to provide 1D/0D behavior [45]. Therefore the verification exercise in this work was done for simpler configurations using 1D and 0D setup. Direct validation data of results through comparison with experiments involving the three-dimensional configuration using radiation as the heat source was not possible. This is because, based on our literature survey, there is no facility that has the capability to study the phenomena in detail. Recent experiments conducted by Pickett et al. [15] and Gallacher et al. [16] are three-dimensional in nature; however, they focused on using convective heating, not radiation. We compared our modeling results with the available experimental data of Pickett et al. [15] and Gallacher et al. [16] with convective heating and the results could be found elsewhere [66,67].

In order to verify the extended BS model, we compared results from [28] with simulations from Gpyro, a one-dimensional version of Gpyro3D without the external gas phase. The configuration consisted of a one dimensional slab of cellulose with thickness of 0.025 m exposed to combined radiative and convective heating on one side and insulated on the other. The radiative and convective temperatures increased from 450 K to 1100 K using a heating rate of 15 K/s, following Ref. [28]. Since [28] did not include moisture, reaction R1 was not included for this validation. The thermophysical properties

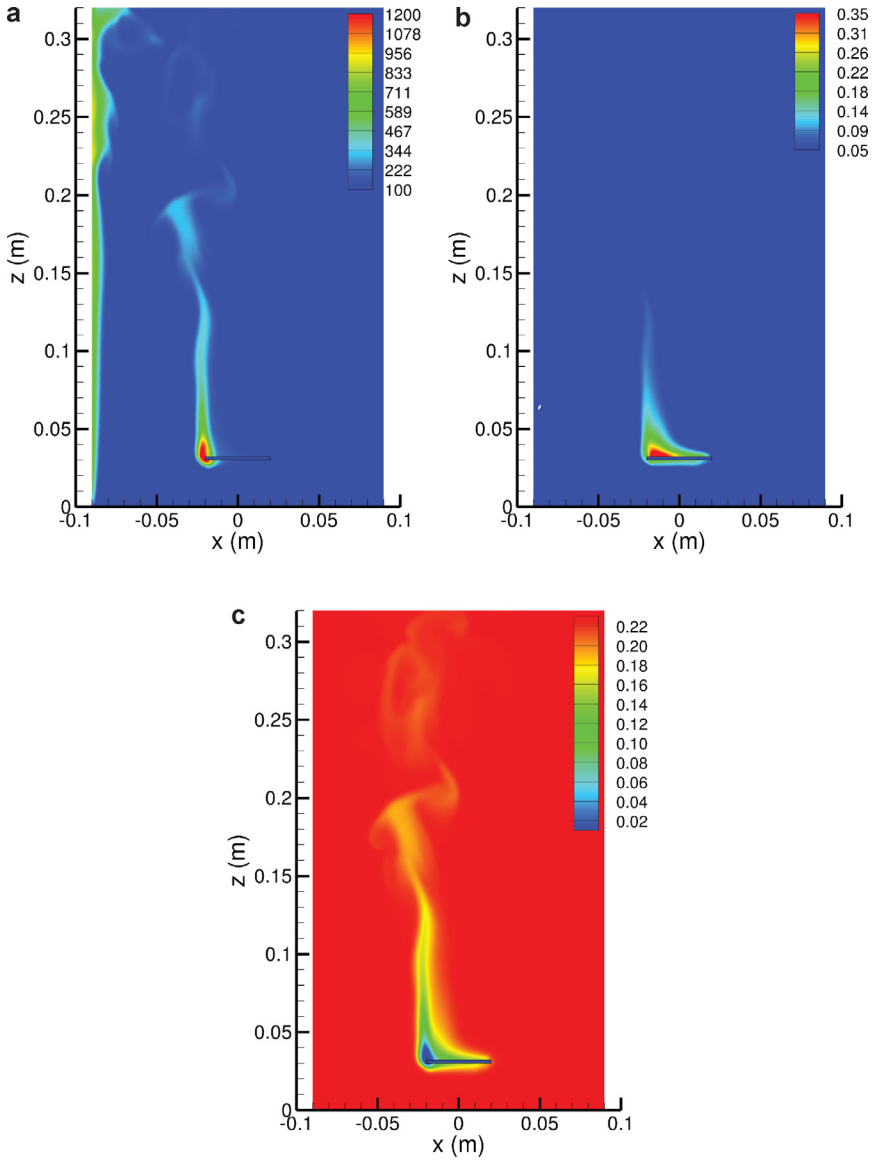

Fig. 13. Gas phase contours of (a) temperature (°C), (b) water vapor mass fraction and (c) oxygen mass fraction at $t = 5$ s on an xz-slice located at $y = 0$ for a case with an initial FMC of 80%.

used for this exercise is given in Table 5 following [28]. Figure 3(a), (b) and (c) illustrates the comparison between temperature, mass concentration of active cellulose and gas phase species velocity along the thickness of the slab at different times. The results of the current study are in reasonably good agreement with Blasi's results [28]. The greatest discrepancy between our model and Blasi's occurred in the simulation of gas phase velocity. We attribute the difference in performance of our model with the original study to unavailable data with respect to the molecular weights and specific heats of gas species in Blasi [28] for which the data pertaining to air has been assumed. Note the abrupt increase and decrease in the concentration of active cellulose Fig. 3(b). Active cellulose formed initially as a result of depolymerization of cellulose; however, due to pyrolysis, it underwent further destruction to char and gas species. The gas phase species velocity, Fig. 3(c), resulted from pressure gradients inside the specimen. The difference in magnitude of velocities in Blasi's and the present study was 0.01 m/s.

In Ref. [68], 0.006 g of cellulose was heated at a rate of 40 K min^{-1} to generate TGA data. These data provided an opportunity to verify the BS model as well. A zero-dimensional version of Gypro with the BS model simulated the TGA data. As seen in Fig. 4, the remaining weight predicted by the model for this setup agreed well with the experimental data [68]. As above, the R1 reaction was omitted in the modeling since the original experiment did not consider a moist specimen.

5. Results and discussions

The classical combustion model for a thermally thin fuel particle assumes that all moisture will first evolve from the sample at a temperature near the boiling point of water [4]. Ignition occurs when a combustible mixture of pyrolysis gases is generated and follows shortly after moisture evaporation is complete [15]. Results from our simulation of the ignition of a modeled leaf by radiation enabled us to test this assumption. The time history of temperature and mass fraction of moisture in the simulated fuel were plotted for a fixed point in Fig. 5 for FMCs of 5%, 40% and 80%. This point was indicated by A in Fig. 2 and located in the solid phase in proximity to the heat source. For a higher FMC, the time at which the temperature rose rapidly was slightly more; the difference in time was less

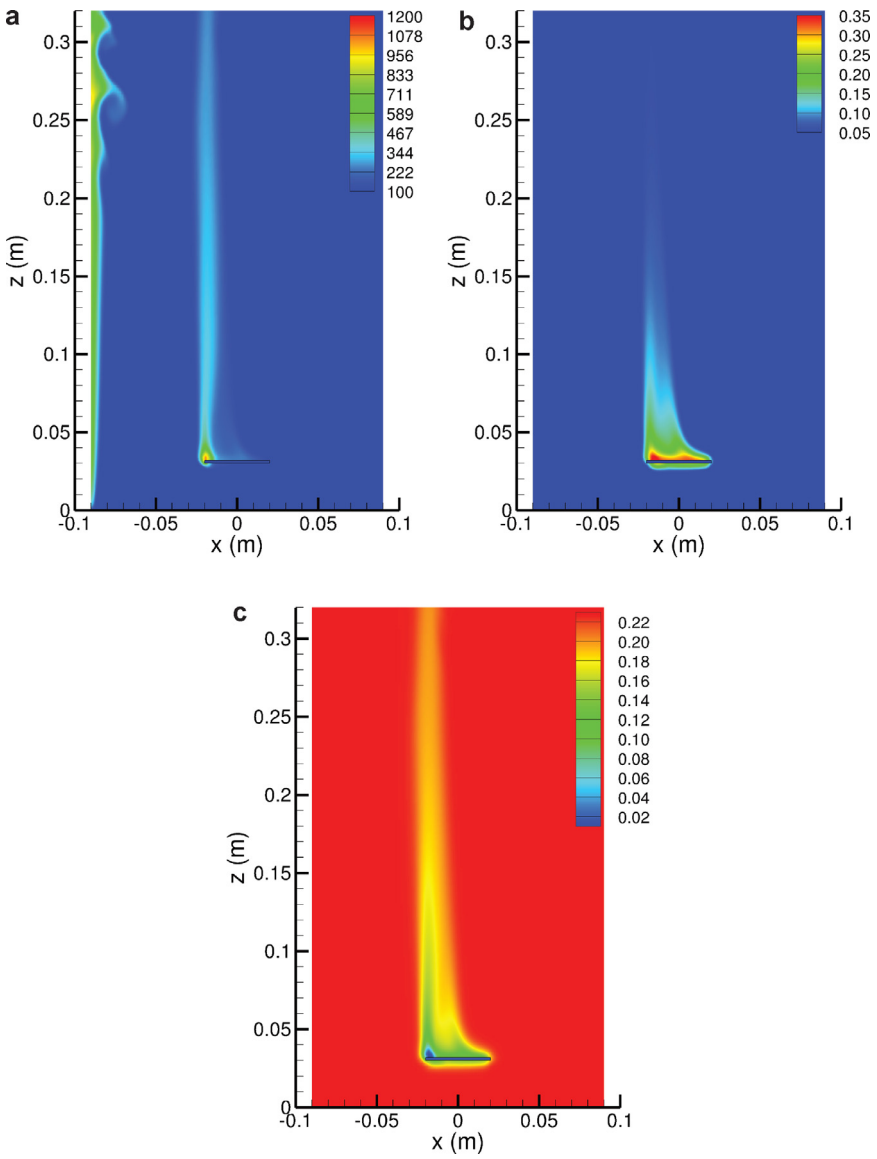

Fig. 14. Gas phase contours of (a) temperature (°C), (b) water vapor mass fraction and (c) oxygen mass fraction along x at $t = 7.5$ s on an xz-slice located at $y = 0$ for a case with an initial FMC of 80%.

than 1 s as seen in Fig. 5(a). This behavior could be attributed to a higher bulk thermal conductivity as the amount of water in the solid fuel increased. Also, as can be seen in this figure, ignition occurred when the temperatures reached 400–500 °C for all the FMC cases. The decay of mass fraction of moisture can be found in Fig. 5(b). Note that the moisture mass fraction is equivalent to the moisture content expressed on a wet mass basis in [37]. Rapid moisture loss occurred first in the driest fuel and last in the fuel with the greatest water content; however, the time at which all moisture was evaporated from the different leaves (cases) differed by 0.8 s. For all the FMC cases, evaporation occured when the temperatures reached 200–300 °C. In order to analyze the temperature and FMC in the solid fuel at a region away from the heat source, temperature and mass fraction distribution of moisture were plotted in Fig. 6 at time 5 s at which gas phase ignition had occurred for 5% FMC case.

It is seen in Fig. 6(a,b) that temperature rise and evaporation of moisture were confined to a local region close to the heat source. The temperature was higher by approximately 700 K for 5% FMC case at the leading edge of the solid fuel. The 40% and 80% cases differed in temperature by less than 50 K in this region and differed by very little along the majority of the solid fuel. Similarly, the temperature for the FMC of 5% decreased by only 100 K over the majority of the solid fuel (−0.017 to 0.02 m). We also observed that a significant amount of moisture remained in the sample at the time of ignition for the 40% and 80% FMC cases. In the area closest to the heat source (−0.02 to −0.016 m), the moisture mass fraction was negligible; however, the mass fraction was unchanged in the region between $x = -0.012$ and 0.02 m, indicating the local evaporation process. In contrast, evaporation occurred in the 5% case along the majority of the fuel length. Also, substantial temperature gradients (250 °C) were observed along the thickness of the solid fuel similar to the gradients reported above. These observations illustrate that the radiative heating can cause non-uniform three dimensional heat transfer within the solid fuel. The local evaporation process discussed above is consistent with the observation made in the experiments of Pickett et al. [15]. They showed time histories of temperature at two points on the surface of manzanita species, one located on the perimeter and the other at the middle of the leaf, and reported that at the perimeter point, evaporation occurred when the temperature was in the range of 200–300 °C. Furthermore, they observed that ignition occurred at

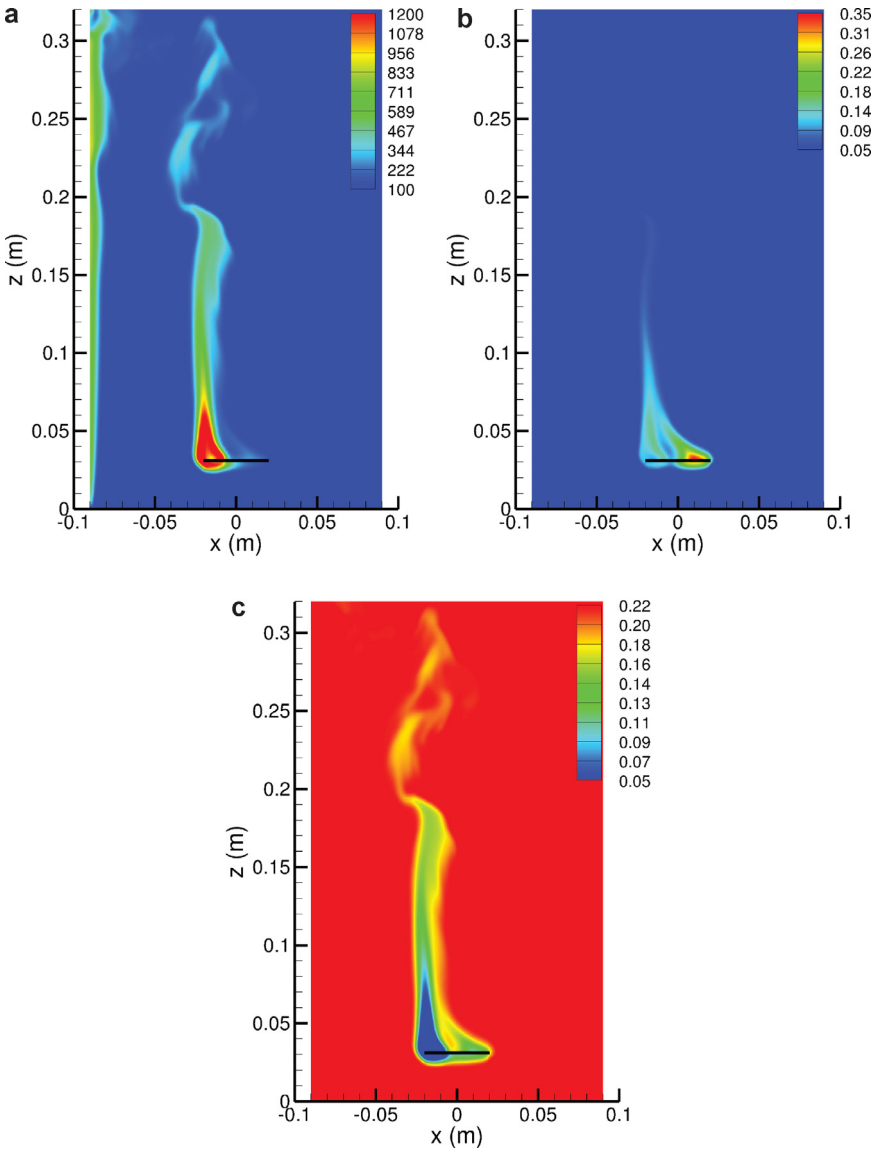

Fig. 15. Gas phase contours of (a) temperature (°C), (b) water vapor mass fraction and (c) oxygen mass fraction along x at $t = 11$ s on an xz-slice located at $y = 0$ for a case with an initial FMC of 80%.

this point after the evaporation process was completed and its temperate reached around 350–400 °C. When the perimeter point ignited, the measured temperature at the middle point was 150 °C. They concluded that a significant amount of moisture was present at the middle when the perimeter point ignited.

The evolution of overall mass loss rate (MLR, rate at which gas species are formed from the solid) and normalized mass (by initial wet mass) is shown in Fig. 7. Water vapor (from evaporation) and fuel vapor (pyrolyzates from active cellulose) comprised the gas species that diffused from the solid phase to the external gas phase domain. The time at which MLR values became positive can be treated as the initiation of pyrolysis which occurred at 2.5 s for FMC of 5%, 40% and 80%. Note that the MLR curves for each of these cases exhibited two overall peaks. The first peak represented water vapor and the second peak represented fuel vapor. As FMC increased, the first peak value increased due to more water vapor being lost during the drying phase. The MLR associated with the second peaks did not differ greatly between three FMC cases and maximum MLR of the second peak ranged from 0.09 to 0.12 g s^{-1}. The normalized mass exhibited a similar trend for all three FMC's.

Oxidation of the gas phase fuel vapors resulted in flaming combustion. Time histories of heat release rate (HRR) and burn rate are shown in Fig. 8 for FMC of 5%, 40% and 80%. HRR quantifies the amount of heat generated by stoichiometric combustion of fuel vapors with oxygen in the gas phase (see Eq. (9)). Here, HRR is used as an indicator of gas phase ignition. As could be seen in Fig. 8(a), FMC affected the time at which ignition occurred. Ignition occurred at $t = 3.5$, 4, and 4.2 s for FMC = 5%, 40%, and 80%, respectively. The second ignition point occurred at 5.75, 8, 10 s for FMC of 5%, 40% and 80%, respectively. Burn rate shows the rate at which the fuel is consumed by the combustion reaction in the gas phase. As seen in Fig. 8(b), the burn rate follows the same trend as the HRR displaying two ignition points.

Now, a detail discussion is made for the evolution of the case with FMC of 80%. The solid fuel degradation model, based on the 5-step extended BS mechanism included four solid and four gas phase species (Eqs. R1–R5). Figures 9(a) and 9(b) display the time history of all solid and gas species, respectively, at point A. The conversion of solid species into gas species during thermal decomposition occurred as follows. In case of solid species, the first degradation reaction occurred near 2.5 s and accounted for phase transformation of moisture

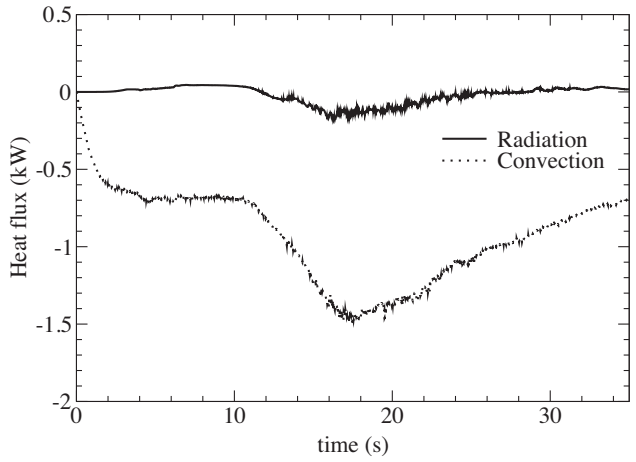

Fig. 16. Time history of global radiation and convection fluxes for a case with FMC of 80%. Positive heat flux means heat is transferred from gas to solid particle and negative heat flux means vice versa.

to water vapor. Seen in Fig. 9(a) is an increase in the mass fraction of cellulose, which is because of the removal of the mass of moisture from the solid phase. Shortly after this, as the temperature of the solid fuel increased, cellulose converted to active cellulose which then later broke down to char, fuel vapors, and tar. Char remained as a residual species in the solid fuel and did not undergo further degradation. It is noted that water vapor formed in the solid and fuel vapors began to evolve even before the water vapor diffused out (Fig. 9(b)). The fuel vapors diffused into the gas phase domain at 5 s which resulted in ignition due to reaction with oxygen at $t = 5$ s. The mass fraction of fuel vapors increased at $t = 10$ s due to diffusion from the neighboring solid phase cells. Tar cracking consumed oxygen; however, it eventually diffused back into the solid from the external gas phase domain.

The spatial variation of moisture mass fraction within the solid fuel along x and y axes is shown at different time instants in Figs. 10(a) and 10(b) in the solid fuel. In Fig. 10(a) a drying front propagated along the length of the solid fuel over time. Two drying fronts propagated transversely from the edges of the solid fuel inward, as seen Fig. 10(b). Evaporation occurred at the edges of the solid fuel at a higher rate than in the center. At $t = 10$ s, local peaks in mass fraction of moisture were observed in regions located closer to the edges of the solid fuel. This resulted from non-uniform heating that arose due to propagation of thermal fronts from the leading edge and the two lateral edges of the solid fuel. At the time of ignition, the solid fuel still contained a large amount of moisture, indicating that different regions in the domain pyrolyzed/ignited at different instants, as shown in Fig. 11(a), (b), (c). High moisture gradients at the leading edge and the two lateral edges indicated a non-uniform evaporation phase during the ignition of the solid fuel in our simulations. This observation is in a general agreement with the observation made by Pickett et al. [15] through the IR measurements.

As described by Byram [39], water vapor in the combustion environment arises from two sources, water contained in the fuel and water produced by the combustion reaction. The simulations tracked H_2O in the gas phase by solving a single transport equation. The mass fractions of H_2O, CO_2, O_2 and fuel vapors immediately above the solid fuel changed along the length of the fuel in x direction. At time 5 s, Fig. 12(a), we observe a reaction zone corresponding to the first ignition point accompanied by products such as water vapor and carbon dioxide at $x = -0.02$ with an oxygen deficient region ahead of the reaction zone at $x - 0.0125$ m characterized by an oxygen mass fraction of 0.11. At time 7.5 s in Fig. 12(b), we observe an increased evaporation ahead of the ignition zone shown by the second peak in mass fraction of water vapor. This resulted in further reduction of oxygen ahead of the ignition zone. The first peak is due to formation of water due to combustion whereas the second peak is due to evaporation of moisture in the solid fuel. In Fig. 12(c) at time 11 s we observe the initiation of another reaction zone corresponding to second ignition point accompanied by negligible oxygen mass fraction. This is due to consumption of oxygen by the combustion reaction. However ahead of this region $x = -0.0075$, oxygen has replenished and this aids the flame spread to other regions of the solid fuel.

To investigate the ignition and flame dynamics further, two-dimensional contours of temperature, volume fraction of oxygen and moisture are plotted on an xz slice located at $y = 0$ in the gas phase domain at times 5 s, 7.5 s and 11 s, shown in Figs. 13–15, respectively. The flaming combustion zone which is represented as the first ignition point in Fig. 13(a) was observed initially at the tip of the solid fuel located close to the heating source. As seen from Fig. 13(b), the water vapor is predominant in the ignition zone as well as in the

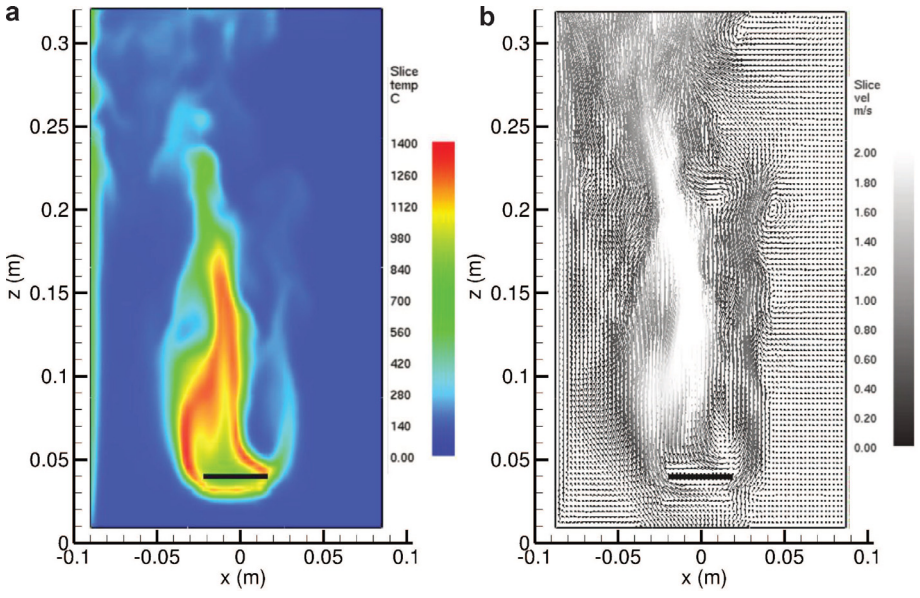

Fig. 17. (a) Gas phase temperature contours (°C), and (b) velocity vectors at time 15 s on an xz-slice located at $y = 0$ for a case with an initial FMC of 80%.

region away from it, indicating that evaporation and combustion occur together. The water vapor present in the ignition zone is a result of combustion; however, its presence ahead of the ignition zone is due to evaporation of moisture from the solid fuel. This released water vapor ahead of the ignition zone, as displayed in Fig. 13(b), causes dilution and consequently, depletion of oxygen, as seen in Fig. 13(c). The ignition zone is reduced at time 7.5 s, as seen in Fig. 14(a), while a high volume fraction of water vapor is observed with oxygen depletion ahead of the ignition zone, as seen in Fig. 14(b, c). At a later time, when most of the water vapor has evaporated in the gas phase domain at $x = 0$ (Fig. 15(b)), a second ignition at the tip of the solid fuel is observed (Fig. 15(a)) and oxygen has replenished ahead of the ignition zone (Fig. 15(b)). Also, seen in Fig. 15(b) is a high mass fraction of water vapor at the trailing edge, indicating that the vapor released during evaporation is significantly more than that formed as a combustion product. The flame created by the second ignition later spreads from the leading edge and the lateral edges towards the trailing edge of the solid fuel.

Figure 16 shows the relative importance of the convection and radiation heat transfer in igniting the solid fuel particle. The negative heat fluxes values observed in case of convection during initial time accounts for the heat transfer between the heated wall and the surrounding gas. However, later in time when the solid fuel ignites, it undergoes cooling through natural convection which results in increased convective heat flux. The positive radiative heat flux observed during the initial time accounts for the radiation energy absorbed by solid fuel from the external gas phase domain. Later when the solid fuel ignites, it emits radiation back into the gas phase which results in negative heat flux as seen from the figure. The role of thermal radiation in causing gas phase ignition has also been investigated by considering many cases where in the solid fuel was being exposed to a heated surface maintained at different temperatures. Ignition was observed only when the temperature of the heated surface was more than 1100 K indicating that thermal radiation can ignite the fuel without the use of a pilot source provided the temperature of the heating source is high enough.

Finally, shown in Fig. 17(a,b) are a contour plot for temperature and velocity vectors in the gas phase, respectively, at $t = 15$ s. From Fig. 17(a), it is observed that the flame is turbulent due to the entrained flow from the external ambient air and due to the interaction with boundary layer developed over the heated wall. Correspondingly, as seen in Fig. 17(b), large scale vortical structures formed as a result of straining between the buoyant plume region and the external air. Furthermore, in the plume region, the plume interaction with boundary layer formed over the heated wall is evident. The Reynolds number (Re) based on the upstream entrainment velocity (0.75 m/s) and the dimension of the solid fuel was close to 1500 at time 16 s, also suggesting that the flow is turbulent [69].

6. Conclusions and future work

The effect of fuel moisture on pyrolysis and combustion of a live vegetation represented as a thin cellulosic fuel element subjected to radiative heating has been investigated using a comprehensive solid-gas coupled model, Gpyro-3D/FDS. A thermal degradation reaction mechanism used for cellulose breakdown was initially verified and validated with previously published simulation and TGA experiments. Fuel moisture content of 5%, 40% and 80% were considered and studied in detail. The temperature response and thermal degradation rate was higher for the case with 5% FMC and ignition occurred prior to the 40% and 80% FMC case. The simulations also indicated that water evaporated locally near the point of ignition and remained elsewhere indicating that different points in the domain evaporate and pyrolyze at different times. Local peaks in the mass fraction of moisture was observed at a region located close to lateral edges of the solid fuel indicating a non-uniform evaporation phase during ignition of the fuel. In the gas phase, high volume fraction of water vapor observed in the region close to the combustion zone as well as away from this region illustrated that evaporation and ignition can occur together. Dilution of oxygen by water vapor ahead of the ignition zone indicated that moisture affected both pyrolysis and gas phase combustion. The initial results of this coupled model are promising. We will use this model to examine the effects of heat transfer method (convection vs. radiation) on ignition of live fuel particles of various shapes and moisture content and compare model results with observed data.

Acknowledgments

The first three authors gratefully acknowledge the financial support of Joint Fire Sciences Program project 11-1-4-19 administered by the USDA Forest Service PSW Research Station through cooperative agreement 11-JV-11272167-103 with The University of Alabama in Huntsville.

References

[1] S.J. Pyne, Fire: A brief history, University of Washington Press, 2001.
[2] D.R. Weise, C.S. Wright, Wildland fire emissions, carbon and climate: Characterizing wildland fuels, Forest Ecol. Manag. 317 (2013) 26–40.
[3] R.M. Nelson Jr., Water relations of forest fuels, in: E. Johnson, K. Miyanishi (Eds.), Forest Fires: Behavior and Ecological Effects, Academic Press, San Diego, CA, 2001, pp. 79–149.
[4] R. Rothermel, A Mathematical Model for Predicting Fire Spread in Wildland Fuels, Research Paper INT-115, U.S. Department of Agriculture, Intermountain Forest and Range Experiment Station, Ogden, UT, 1972.
[5] P. Andrews, BEHAVE: Fire Behaviour Prediction and Fuel Modelling System – BURN Subsystem. Part 1, General Technical Report INT-194, U.S. Department of Agriculture, Forest Service, Intermountain Forest and Range Experiment Station, Ogden, UT, 1986.
[6] M.A. Finney, FARSITE Fire Area Simulator: Model Development and Evaluation, Special Publication RMRS-RP-4, U.S. Department of Agriculture, Forest Service, Rocky Mountain Research Station, 1998.
[7] A.L. Sullivan, Wildland surface fire spread modelling, 1990-2007. 1: Physical and quasi-physical models, Int. J. Wildland Fire 18 (4) (2009) 349–368.
[8] A.L. Sullivan, Wildland surface fire spread modelling, 1990-2007. 2: Empirical and quasi-empirical models, Int. J. Wildland Fire 18 (4) (2009) 369–386.
[9] A.L. Sullivan, Wildland surface fire spread modelling, 1990-2007. 3: Simulation and mathematical analogue models, Int. J. Wildland Fire 18 (4) (2009) 387–403.
[10] P.J. Pagni, T.G. Peterson, Flame spread through porous fuels, Symp. (Int.) Combust. 14 (1) (1973) 1099–1107.
[11] J. Balbi, P. Santoni, J. Dupuy, Dynamic modelling of fire spread across a fuel bed, Int. J. Wildland Fire 9 (4) (1999) 275–284.
[12] X. Zhou, S. Mahalingam, D.R. Weise, Modeling of marginal burning state of fire spread in live chaparral shrub fuel bed, Combust. Flame 143 (3) (2005) 183–198.
[13] K.M. Yedinak, J.D. Cohen, J.M. Forthofer, M.A. Finney, An examination of flame shape related to convection heat transfer in deep-fuel beds, Int. J. Wildland Fire 19 (2) (2010) 171–178.
[14] S. McAllister, I. Grenfell, A. Hadlow, W. Jolly, M. Finney, J. Cohen, Piloted ignition of live forest fuels, Fire Saf. J. 51 (2012) 133–142.
[15] B.M. Pickett, C. Isackson, R. Wunder, T.H. Fletcher, B.W. Butler, D.R. Weise, Experimental measurements during combustion of moist individual foliage samples, Int. J. Wildland Fire 19 (2010) 153–162.
[16] J.R. Gallacher, V. Lansinger, S. Hansen, D. Jack, D.R. Weise, T.H. Fletcher, Effects of Season and Heating Mode on Ignition and Burning Behavior of Three Species of Live Fuel Measured in a Flat-flame Burner System, Spring Technical Meeting of the Western States Section of the Combustion Institute, Pasadena, CA, 2014.
[17] J.D. Engstrom, J.K. Butler, S.G. Smith, L.L. Baxter, T.H. Fletcher, D.R. Weise, Ignition behavior of live California chaparral leaves, Combust. Sci. Technol. 176 (9) (2004) 1577–1591.
[18] F. Shafizadeh, The chemistry of pyrolysis and combustion, American Chemical Society, 1984, pp. 489–529.
[19] V. Babrauskas, Ignition Handbook, Fire Science Publishers, Issaquah, WA, 2003.
[20] M. Kokkala, D. Baroudi, A thermal model for upward flame spread on a combustible wall, Technical Report, Valtion Teknillinen Tutkimuskeskus, Espoo, Finland, 1993.
[21] N. Boonmee, J.G. Quintiere, A theoretical investigation of surface glowing ignition leading to gas flaming autoignition, in: Proceedings of the 8th International Symposium on Fire Safety Science, 2005, pp. 139–150.
[22] H. Yang, R. Yan, H. Chen, D.H. Lee, C. Zheng, Characteristics of hemicellulose, cellulose and lignin pyrolysis, Fuel 86 (2007) 1781–1788.
[23] K.W. Ragland, D.J. Aerts, Properties of wood for combustion analysis, Bioresour. Technol. 37 (1991) 161–168.
[24] A.J. Stamm, Thermal degradation of wood and cellulose, Ind. Eng. Chem. 48 (3) (1956) 413–417.
[25] D. Meier, O. Faix, State of the art of applied fast pyrolysis of lignocellulosic materials a review, Bioresour. Technol. 68 (1) (1999) 71–77.

[26] M. Brebu, C. Vasile, Thermal degradation of lignin - a review, Cellul. Chem. Technol. 44 (9) (2010) 353–363.
[27] J. Ld, Cellulose pyrolysis kinetics: An historical review on the existence and role of intermediate active cellulose, J. Anal. Appl. Pyrolysis 94 (2012) 17–32.
[28] C.D. Blasi, Numerical simulation of cellulose pyrolysis, Biomass Bioenergy 7 (1-6) (1994) 87–98.
[29] F.J. Kilzer, A. Broido, Speculations on the nature of cellulose pyrolysis, Pyrodynamics 2 (1965) 151–163.
[30] P. Chatterjee, C. Conrad, Kinetics of the pyrolysis of cotton cellulose, Textile Res. J. 36 (1966) 487–494.
[31] F. Shafizadeh, Pyrolytic Reactions and Products of Biomass, Springer Netherlands, Dordrecht, 1985, pp. 183–217.
[32] R. Capart, L. Khezami, A.K. Burnham, Assessment of various kinetic models for the pyrolysis, Thermochim. Acta 417 (2004) 79–89.
[33] P. Lewellen, W. Peters, J. Howard, Cellulose pyrolysis kinetics and char formation mechanism, Symp. (Int.) Combust. 16 (1) (1977) 1471–1480.
[34] A.G.W. Bradbury, Y. Sakai, F. Shafizadeh, A kinetic model for pyrolysis of cellulose, J. Appl. Polym. Sci. 23 (1979) 3271–3280.
[35] N. Bech, M.B. Larsen, P.A. Jensen, K.D. Johansen, Modelling solidconvective flash pyrolysis of straw and wood in the pyrolysis centrifuge reactor, Biomass Bioenergy 33 (2009) 999–1011.
[36] C.M. Countryman, Moisture in living fuels affects fire behavior, Fire Manag. Notes 35 (2) (1974) 10–14.
[37] W.M. Jolly, A.M. Hadlow, K. Huguet, De-coupling seasonal changes in water content and dry matter to predict live conifer foliar moisture content, Int. J. Wildland Fire 23 (4) (2014) 480.
[38] V. Tihay, P. Gillard, Pyrolysis gases released during the thermal decomposition of three mediterranean species, J. Anal. Appl. Pyrolysis 88 (2) (2010) 168–174.
[39] G.M. Byram, Combustion of forest fuels, in: K. Davis (Ed.), Forest Fire: Control and Use, McGraw-Hill, New York, 1959, pp. 61–89.
[40] S.C. Ferguson, A. Dahale, B. Shotorban, S. Mahalingam, D.R. Weise, The role of moisture on combustion of pyrolysis gases in wildland fires, Combust. Sci. Technol. 185 (2013) 435–453.
[41] M. Janssens, Piloted ignition of wood: a review, Fire Mater. 15 (4) (1991) 151–167.
[42] D.L. Simms, M. Law, The ignition of wet and dry wood by radiation, Combust. Flame 11 (5) (1967) 377–388.
[43] M. Abu-Zaid, Effect of Water on Ignition of Cellulosic Materials (Ph.D. thesis), Michigan State University, East Lancing, MI, 1988.
[44] B.M. Jenkins, L.L. Baxter, T.R.M. Jr, T.R. Miles, Combustion properties of biomass, Fuel Process. Technol. 54 (1998) 17–46.
[45] C.W. Lautenberger, Gpyro3D: A three dimensional generalized pyrolysis model, Proceedings of International Symposium on Fire Safety Science, IAFSS, 2014.
[46] K. McGrattan, S. Hostikka, J. Floyd, H. Baum, R. Rehm, W. Mell, R. McDermott, Fire Dynamics Simulator (Version 5): Technical Reference Guide, Special Publication 1018-5, U.S. Department of Commerce, National Institute of Standards and Technology, 2007.
[47] K. McGrattan, R. McDermott, S. Hostikka, J. Floyd, Fire Dynamics Simulator (Version 5): User's Guide, Special Publication 1019-5, U.S. Department of Commerce, National Institute of Standards and Technology, 2007.
[48] B. Magnussen, B. Hjertager, On mathematical modeling of turbulent combustion with special emphasis on soot formation and combustion, Symp. (Int.) Combust. 16 (1) (1977) 719–729.
[49] K. McGrattan, S. Hostikka, R. McDermott, J. Floyd, C. Weinschenk, K. Overholt, Fire Dynamics Simulator Technical Reference Guide Volume 1: Mathematical Model, Special Publication 1018-6, U.S. Department of Commerce, National Institute of Standards and Technology, 2013.
[50] W. Mell, A. Maranghides, R. McDermott, S.L. Manzello, Numerical simulation and experiments of burning douglas fir trees, Combust. Flame 156 (10) (2009) 2023–2041.
[51] N. Peters, Theoretical and numerical combustion, Cambridge University Press/John Wiley and Sons, Cambridge, UK, 2000.
[52] T. Poinsot, D. Veynante, Turbulent Combustion, second ed., Edwards, 2005.
[53] A. Dahale, S. Ferguson, B. Shotorban, S. Mahalingam, Effects of distribution of bulk density and moisture content on shrub fires, Int. J. Wildland Fire 22 (5) (2013) 625–641.
[54] W. Grosshandler, RadCal: A Narrow Band Model for Radiation Calculations in a Combustion Environment, NIST Technical Note TN 1402, National Institute of Standards and Technology, Gaithersburg, Maryland, 1993.
[55] W. Mell, A. Maranghides, R. MecDermott, S.L. Manzello, Numerical simulation and experiments of burning douglas fir trees, Combust. Flame 156 (2009) 2023–2041.
[56] C.P. Bankston, B.T. Zinn, R.F. Browner, E.A. Powells, Aspects of the mechanisms of smoke generation by burning materials, Combust. Flame 41 (1981) 273–292.
[57] G.D. Raithby, E.H. Chui, A finite-volume method for predicting radiant heat transfer in enclosures with participating, J. Heat Transfer 112 (2) (1990) 415–423.
[58] J.P. Holman, Heat transfer, seventh ed., McGraw-Hill, New York, 1990.
[59] R. Bird, W. Stewart, E. Lightfoot, Transport Phenomena, Revised 2nd ed., John Wiley and Sons, New York, 2007.
[60] L. Thomas, Elliptic problems in linear differential equations over a network, report, Columbia University, Watson Scientific Computing Laboratory, New York, NY, 1949.
[61] K.M. Bryden, K.W. Ragland, C.J. Rutland, Modeling thermally thick pyrolysis of wood, Biomass Bioenergy 22 (2002) 41–53.
[62] R.J. Ross, Wood Handbook, General Technical Report FPLGTR190, Forest Products Laboratory, United States Department of Agriculture Forest Service, 2010.
[63] B.W. Butler, J. Cohen, D.J. Latham, R.D. Schuette, P. Sopko, K.S. Shannon, D. Jimenez, L.S. Bradshaw, Measurements of radiant emissive power and temperatures in crown fires, Can. J. Forest Res. 34 (8) (2004) 1577–1587.
[64] S.B. Pope, Ten questions concerning the large-eddy simulation of turbulent flows, New J. Phys. 6 (1) (2004) 35.
[65] K. Hill, J. Dreisbach, F. Joglar, B. Najafi, K. McGrattan, R. Peacock, A. Hamins, Verification and Validation of Selected Fire Models for Nuclear Power Plant Applications: Fire Dynamics Simulator vol. 7, Final Report NUREG-1824, U.S. Nuclear Regulatory Commission, Office of Nuclear Regulatory Research, 2007.
[66] B.L. Yashwanth, B. Shotorban, S. Mahalingam, A computational investigation of the role of moisture in live fuels subject to pyrolysis and ignition through convective heat transfer, Proceedings of the 9th US National Meeting, Central States Section of the Combustion Institute, Cincinnati, OH, 2015.
[67] B.L. Yashwanth, J. Gallacher, B. Shotorban, S. Mahalingam, T.H. Fletcher, D.R. Weise, Experimental and numerical investigation of the effect of heating modes and moisture content on pyrolysis and ignition of live fuels, Proceedings of the 9th US National Meeting, Central States Section of the Combustion Institute, Cincinnati, OH, 2015.
[68] J.P. Diebold, A unified, global model for the pyrolysis of cellulose, Biomass Bioenergy 7 (1994) 75–85.
[69] V.D. Narasimhamurthy, H.I. Andersson, Numerical simulation of the turbulent wake behind a normal flat plate, Int. J. Heat Fluid Flow 30 (6) (2009) 1037–1043.
[70] L.J. Curtiss, D.J. Miller, Transport model with radiative heat transfer for rapid cellulose pyrolysis, Ind. Eng. Chem. Res. 27 (1988) 1775–1783.